Monthly Notices of the ROYAL ASTRONOMICAL SOCIETY

MNRAS **520,** 1005–1021 (2023) https://doi.org/10.1093/mnras/stad202
Advance Access publication 2023 January 19

On the density regime probed by HCN emission

Gerwyn H. Jones [1]★ Paul C. Clark [1] Simon C. O. Glover [2] and Alvaro Hacar[3]

[1]*School of Physics and Astronomy, Queen's Buildings, The Parade, Cardiff University, Cardiff, CF24 3AA*
[2]*Zentrum für Astronomie der Universität Heidelberg, Institut für Theoretische Astrophysik, Albert-Ueberle-Str 2, D-69120 Heidelberg, Germany*
[3]*University of Vienna, Department of Astrophysics, Türkenschanzstrasse 17, A-1180 Vienna, Austria*

Accepted 2023 January 16. Received 2023 January 16; in original form 2021 December 9

ABSTRACT

HCN $J = 1$–0 emission is commonly used as a dense gas tracer, thought to mainly arise from gas with densities $\sim 10^4$–10^5 cm^{-3}. This has made it a popular tracer in star formation studies. However, there is increasing evidence from observational surveys of 'resolved' molecular clouds that HCN can trace more diffuse gas. We investigate the relationship between gas density and HCN emission through post-processing of high-resolution magnetohydrodynamical simulations of cloud–cloud collisions. We find that HCN emission traces gas with a mean volumetric density of $\sim 3 \times 10^3$ cm^{-3} and a median visual extinction of $\sim$5 mag. We therefore predict a characteristic density that is an order of magnitude less than the 'standard' characteristic density of $n \sim 3 \times 10^4$ cm^{-3}. Indeed, we find in some cases that there is clear HCN emission from the cloud even though there is no gas denser than this standard critical density. We derive independent luminosity-to-mass conversion factors for the amount of gas at $A_V > 8$ or at densities $n > 2.85 \times 10^3$ cm^{-3} or $n > 3 \times 10^4$ cm^{-3}, finding values of $\alpha_{\rm HCN} = 6.79$, 8.62, and 27.98 M$_\odot$(K km s^{-1} pc^2), respectively.

Key words: stars: formation – ISM: clouds – ISM: molecules – galaxies: ISM.

1 INTRODUCTION

A central goal of star formation theory is to predict the rate at which gas in the interstellar medium (ISM) is converted into stars, and so research into this field has focused on measuring the amount of gas present to form stars, and connecting that to the amount of star formation that actually occurs. Perhaps the most widely-studied relation is that between the surface density of the star formation rate, and the surface density of gas, known as the Kennicutt–Schmidt (K–S) relation (Schmidt 1959; Kennicutt 1989),

$$\Sigma_{\rm SFR} \propto \Sigma_{\rm gas}^{\rm N}. \quad (1)$$

Kennicutt (1989) found N to be 1.4 ± 0.15, however there has been some debate over the value of the index since (Bigiel et al. 2010; Shetty et al. 2014). Simple arguments for the KS relation have been presented by several authors (Elmegreen 1994; Wong & Blitz 2002; Krumholz & Tan 2007), revolving around the idea that a roughly constant fraction of the gas present in molecular clouds will be converted into stars each free-fall time. With $t_{\rm ff} \propto \rho^{-0.5}$, we would expect $\dot{\rho} \propto \rho^{1.5}$ and with an assumption that scale heights of galaxies do not vary significantly, we can come to the conclusion that $\Sigma_{\rm SFR} \propto \Sigma_{\rm gas}^{1.5}$.

However, the interpretation of the K–S relation is more complicated when we start to consider what 'gas available for star formation' actually means. The early study by Kennicutt (1989) used CO emission to trace the gas surface density. Later studies (Bigiel et al. 2010; Shetty et al. 2014) that also focus on CO emission suggested lower values of the K–S index, towards $N \approx 1$ (although this too is under debate: Kennicutt & Evans 2012).

As one moves to progressively higher density gas tracers, one would expect the correlation between the mass of the gas present and star formation rate to become tighter, provided that the star formation is being measured on time-scales similar to the free-fall time of the gas tracer (see the work by Kruijssen et al. (2014) for a discussion of the time-scales). For example, Gao & Solomon (2004a), Gao & Solomon (2004b) conducted a K–S study using HCN $J = 1$–0[1] line emission, which is assumed to trace higher density gas than CO, and found that $L_{\rm FIR} \propto L_{\rm HCN}$. This implies that $\Sigma_{\rm SFR} \propto \Sigma_{\rm gas}$, and so for HCN emission the K–S index is around 1. Wu et al. (2005) suggested that the HCN emission from a galaxy simply counts the number of star-forming clumps present in these galaxies, and so HCN is primarily tracing the densities at which star formation 'sets in'. This has spawned significant interest in HCN as a tracer of 'dense gas' in the ISM, and as a tool for studying the star formation relations in more detail.

However, exactly what density HCN traces is still very much unclear. Although the critical density is quite high – $n_{\rm crit} = 4.7 \times 10^5$ cm^{-3} for the multilevel definition of the critical density at 10 K – the line is typically optically thick, which can lower the effective critical density, as discussed in detail by Shirley (2015). Indeed, Shirley (2015), using simple one-dimensional radiative transfer, demonstrates that a 1 K km s^{-1} line can be produced by densities as low as 8.4×10^3 cm^{-3}, due to radiative trapping. This is below the density that HCN was assumed to trace in the studies of

[1]Note that we will refer to 'HCN $J = 1$–0' simply as 'HCN' for the rest of the paper

★ E-mail: Gerwyn.Jones@astro.cf.ac.uk

Gao & Solomon (2004a), Gao & Solomon (2004b), where they calculated that HCN emission was probing a characteristic density of 3×10^4 cm^{-3}.

Krumholz & Thompson (2007) investigated how the KS law changes with differing molecular gas tracers, including HCN (Nguyen et al. 1992; Gao & Solomon 2004a, b; Riechers et al. 2006; Gao et al. 2007). Similar to Gao & Solomon (2004b), their model uses an LVG calculation but with the inclusion of a lognormal PDF for the density in the molecular gas in their model. With this approach they found that HCN emission generally traces dense gas, $n_{\rm dense} \sim 10^5$ cm^{-3}. Their model showed a strong correlation with the observed data with a direct proportionality between far infrared luminosity and HCN luminosity.

More recently, Leroy et al. 2017 have used LVG calculations to explore the influence of the density PDF on the characteristic density traced by HCN emission. They found that the characteristic density is highly sensitive to what one assumes regarding the cloud density PDF, with values from their models ranging from $\sim 10^3$ cm^{-3} to more than 10^5 cm^{-3}. However, one weakness of this and the other simple models described above is that they incorporate little or no information on the spatial distribution of the dense gas, which potentially has a large impact on the relation between HCN optical depth and gas density. A first attempt to properly account for the spatial structure of the dense gas was made by Onus, Krumholz & Federrath 2018, who post-processed a high resolution simulation of a small portion of a molecular cloud by Federrath 2015. Based on this calculation, they predicted that HCN emission traces gas with a luminosity-weighted mean density of $0.8–1.7 \times 10^4$ cm^{-3}.

There is also increasing evidence from observational studies of giant molecular clouds (GMCs) in the Milky Way that HCN is probing lower densities than previous assumed. Pety et al. (2017), Kauffmann et al. (2017), and Barnes et al. (2020) have shown that HCN also traces diffuse regions of molecular clouds at a density of $\sim$500, $\sim 10^3$, $\sim 10^{-3}$ cm, respectively. Tafalla, Usero & Hacar (2021) also show that HCN emission can be detected at visual extinctions ($A_{\rm V}$) as low as $\sim$1 mag.

In this paper, we will expand upon the work of Onus et al. (2018). First, rather than simulating a small subregion within a cloud, we will use simulations of low-density 'cloud–cloud collisions', to create dense molecular regions with self-consistent density and velocity fields. Second, we will use a detailed model of the heating and cooling processes that is coupled to a time-dependent chemical network that follows H_2 and CO formation and destruction. Although we do not follow the HCN chemistry self-consistently in our study, we will use the results from Fuente et al. (2019) to relate the HCN abundance at each point in the simulation volume to the CO abundance and the local visual extinction – two properties that are followed self-consistently in our simulations. We perform radiative transfer (RT) post-processing on the simulations with the publicly available code RADMC-3D (Dullemond et al. 2012) to make synthetic observations of the HCN (1–0) line, and we use these to explore the density regime traced by HCN emission. Where possible, we have compared to the recent observational studies.

In Section 2, we describe in detail the magnetohydrodynamical simulations that form the basis of this study, and the radiative transfer post-processing that we perform to get the synthetic HCN emission cubes. We present the basic evolution of the magnetohydrodynamical simulations in Section 3, and discuss how we decide when in the cloud evolution we perform the RT. The HCN emission is presented in Section 4, including the discussion of the density regime that it probes in our simulations. We relate HCN (1–0)/CO (1–0) to dense gas in section 5. We discuss some possible caveats in our study in Section 6 and present our conclusions in Section 7.

2 NUMERICAL APPROACH

We investigate two spherical clouds that collide head-on at four different velocities using a magnetohydrodynamical (MHD) code that includes a time-dependent chemical network for H_2 and CO formation, which runs alongside a detailed treatment of the heating and cooling in the ISM. We then post-process our simulations using a synthesized HCN abundance, which is related to the CO abundance in our models (see Section 2.3 for further details), and a radiative transfer code to create HCN emission position–position-velocity (PPV) cubes. These are then analysed to determine the density regime traced by HCN emission.

2.1 The numerical model

We use a modified version of the publicly available moving-mesh code, AREPO (Springel 2010; Weinberger, Springel & Pakmor 2020). The adpative moving mesh in AREPO allows us complete control over the resolution in our simulations, while at the same time minimizing advection errors. It is thus ideally suited to this type of ISM problem. Our modifications to AREPO include: the use of the radiative heating and cooling and cosmic ray heating treatments described by Glover & Mac Low (2007), Glover & Clark (2012); the TREECOL algorithm developed by Clark, Glover & Klessen (2012) to calculate the attenuation of the interstellar radiation field (ISRF); time-dependent chemistry that follows H_2 and CO formation (see Hunter et al. 2021); a sink particle algorithm (Bate, Bonnell & Price 1995; Federrath et al. 2010) to treat small, gravitationally-collapsing regions associated with star formation (Tress et al. 2020; Wollenberg et al. 2020).

2.2 Initial conditions

Our simulations start with two spherical clouds, each with a radius of 19.04 pc, a number density of 10 cm^{-3} (note that we will refer to 'number density' simply as 'density' for the rest of the paper) and a mass of 1×10^4 M$_\odot$. Both clouds have an initial temperature of 300 K, consistent with the balance between fine structure cooling and photoelectric heating at a number density of 10 cm^{-3}. The geometry of the simulation is such that the cloud centres are placed at a distance of 57.11 and 114.23 pc, respectively in x, while both centres are placed at a distance of 85.67 pc in both y and z in a cuboid of size 171.34 pc. The velocity of each cloud is mirrored along x such that they are sent on a collision course with one another. Four different velocities are chosen to cover the typical and extremes of the velocity distribution of the gas flow in spiral arms (Dobbs 2008); 1.875, 3.75, 7.5, 15 km s^{-1} (note that these quoted velocities are the velocities of the individual clouds, i.e. the relative velocity is twice these values). An initial turbulent velocity field is applied to the clouds, which follows a P(k) $\propto k^{-4}$ scaling law with a natural mix of solenoidal to compressive modes. The velocity dispersion of the turbulence is set to 1.16 km s^{-1}, which provides virial balance between the (bulk) kinetic and gravitational energies. By allowing a period of time between the initial set-up and the cloud collision, the supersonic turbulence (Mach number of $\sim$2) has the chance to create structure in the clouds before they encounter the main collisional shock.

Each cloud is initially modelled with 2 000 000 cells, randomly generated in a sphere, such that the initial cell mass is 0.005 M$_\odot$. A further 262 144 cells, with mass 0.066 M$_\odot$ are randomly injected into

the rest of the computational domain to model the background gas, which is taken to have a density of $0.063\,\mathrm{cm}^{-3}$. As the simulation progresses, the mesh is constantly monitored to maintain a cell mass of roughly $0.005\,\mathrm{M}_{\odot}$. On top of this, we impose three further resolution criteria. The first criterion is that the Jeans length is resolved by at least 16 cells to make sure we correctly capture the fragmentation in the gas. The second criterion is that the volume of neighbouring cells differs by no more than a factor of 8. Finally, we set a minimum and maximum cell size of 100 au and 12 pc, respectively.

Due to self-gravity in AREPO, the gas in our simulations has the ability to form regions of high density that can undergo runaway gravitational collapse. The final outcome of such a process would be the formation of a star or small stellar system. We employ sink particles (Bate et al. 1995) to model these objects, and to follow both their dynamics and further accretion. In this study, several conditions must be met for a gas cell to be turned into a sink particle, which follows the criteria laid out in Federrath et al. (2010). First, the candidate cell must be above our sink creation density $n_{\mathrm{sink}} = 10^8\,\mathrm{cm}^{-3}$, and be a local minimum in the gravitational potential. Then we require that the gas within the sink accretion radius, r_{sink} – here taken to be 185 au – must be gravitationally bound, and both moving towards and accelerating towards the candidate's location – that is, the mass-weighted $\nabla \cdot \mathbf{v}$ and $\nabla \cdot \mathbf{a}$ within the sink creation radius must be negative).

We make use of the magnetohydrodynamical module in AREPO, as described in Pakmor, Bauer & Springel (2011). This includes hyperbolic divergence cleaning (Dedner et al. 2002) and the divergence advection terms introduced by Powell et al. (1999). In our initial set-up, we include a uniform magnetic field of strength 3 μG, directed along x such that the collision is occurring along the magnetic field lines. This value of 3 μG is consistent with that found from observations of clouds with number densities similar to those we study here (Crutcher et al. 2010; Crutcher 2012).

We adopt a composition characteristic of the local ISM for the metals and dust included in our ISM model (i.e. the heating and cooling and time-dependent chemistry). The initial abundances of carbon and oxygen are set to $x_{\mathrm{C}} = 1.4 \times 10^{-4}$ and $x_{\mathrm{O}} = 3.2 \times 10^{-4}$, respectively, as given by Sembach et al. (2000), where x_i is the fractional abundance of the element relative to hydrogen nuclei. We assume that the carbon starts in the form of C^+ due to the photoionization by the ISRF, and that oxygen starts in the form of neutral oxygen. We also assume that most of the hydrogen starts in atomic form, and that a small amount of hydrogen is in H^+ form ($x_{\mathrm{H}^+} \sim 0.01$) due to the balance of cosmic ray ionization and recombination.

For our model of the interstellar radiation field (ISRF), we adopt the spectral shape described in Mathis, Mezger & Panagia (1983) at longer wavelengths and Draine (1978) at UV wavelengths. The strength of the ISRF is $G_0 = 1.7$ in Habing (1968) units (see Draine 2011) and the cosmic ray ionization rate of atomic hydrogen is set to $\zeta_{\mathrm{H}} = 3 \times 10^{-17}\,\mathrm{s}^{-1}$.

2.3 Radiative transfer post-processing

We use the RADMC-3D radiative transfer (RT) code (Dullemond et al. 2012) to create post-processed position–position-velocity (PPV) cubes of HCN emission from our AREPO simulations. We make use of internal functions in AREPO to create a regular Cartesian grid of fluid properties that can be converted to a form that is compatible with the fixed Cartesian grid used by RADMC-3D. This means, however, that we cannot perform the RT post-processing on the entire computational domain that is evolved in AREPO. We therefore limit our RT analysis to a 10 pc cubic region that envelopes the highest density region in the cloud–cloud collision; AREPO's voronoi mesh is interpolated on to a 450^3 grid such that we have a spatial resolution of 0.022 pc in the RT. This is sufficient to capture both the scales of the molecular cloud and the cores that form within.

Due to the complex nature of nitrogen chemistry, it is currently computationally intractable to self-consistently compute the time-dependent abundance of HCN in our AREPO chemical network. We therefore make use of the observationally-derived $x_{\mathrm{HCN}}/x_{\mathrm{CO}}$ versus A_{V}relation shown in Figure 8 of Fuente et al. (2019). Note that other interpretations of the data in Fuente et al. (2019) are possible. For example from their Figure 6, one could infer that x_{HCN} is proportional to A_{V} above $A_{\mathrm{V}} \approx 10$, and flat below this. However by tying the HCN abundance to the CO abundance, we can capture (phenomenologically) the effects of the photodestruction of the HCN by the ISRF, and thus avoid spuriously large HCN abundances at low densities and A_{V}.

When using the $x_{\mathrm{HCN}}/x_{\mathrm{CO}}$ versus A_{V} relation in Fuente et al (2019), our visual extinction is calculated along the same line of sight as the rays used to solve the RT problem in RADMC-3D, simply by first getting the column density at each point via,

$$N_{\mathrm{H}} = \sum_{i=0}^{N_{\mathrm{LoS}}} \frac{\rho_i}{1.4\,\mathrm{m_p}}\,\Delta L, \tag{2}$$

where i denotes each of the N_{LoS} cells along the line of sight with densities ρ_i and length ΔL; the term $1.4\,m_{\mathrm{p}}$ converts to the number density of hydrogen nuclei. We then convert this to a visual extinction via,

$$A_{\mathrm{V}} = \frac{N_{\mathrm{H}}}{1.87 \times 10^{21}\,\mathrm{cm}^{-2}}, \tag{3}$$

where N_{H} is the column number density of hydrogen *nuclei* (Bohlin, Savage & Drake 1978; Draine & Bertoldi 1996). The column density thus derived is designed to mimic the observed column density used in Figure 8 of Fuente et al. (2019). Note that this differs from the column density as seen by each cell in our simulation, which is derived via our TREECOL algorithm.

Using this relationship, our computed CO abundances derived using AREPO can then be used to calculate our HCN abundance with respect to hydrogen nuclei. We then compute the HCN abundance in each RADMC-3D grid cell via,

$$x_{\mathrm{HCN}} = \Phi(A_{\mathrm{V}}) \cdot x_{\mathrm{CO}}, \tag{4}$$

where $\Phi(A_{\mathrm{V}})$ is our conversion factor from CO abundance to HCN abundance, x_{HCN} is the abundance of HCN relative to hydrogen nuclei, and x_{CO} is the abundance of CO also relative to hydrogen nuclei. The value of $\Phi\,(A_{\mathrm{V}})$ is obtained from the Fuente et al. (2019) results, and we present the data used in Fig. 1. Note that the data in Fuente et al. (2019) covers a limited range in A_{V}. Rather than make up a relation outside these limits, we simply hold the conversion factor constant with increasing/decreasing A_{V}. While one might expect this to cause problems at low A_{V} – potentially boosting the HCN abundance – in practise this does not happen, as at low A_{V} the CO abundance in any case self-consistently falls to zero due to our treatment of the photodissociation. Note that another caveat in our model is that the HCN formation time-scale is assumed to be exactly equivalent to the CO formation time-scale. Although this is unlikely to be exactly the case, the recent results from Priestley & Whitworth (2021) – which captured the non-equilibrium chemistry of a dynamically evolving cloud – demonstrate that both the CO and HCN formation time-scales are shorter than the dynamical time-

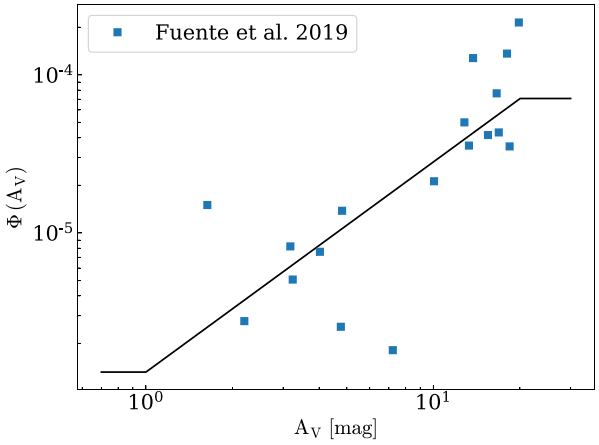

Figure 1. Our conversion factor from CO abundance to HCN abundance, $\Phi\,(A_V)$ (black line), together with the observational measurements of the HCN to CO ratio presented in Fuente et al. 2019 (blue squares).

scale in scenarios similar to those we study here. Thus our coupling of the HCN abundance to the CO abundance is unlikely to affect the results. Priestley & Whitworth (2020) found that a large variation in the distribution of the HCN abundance in the density space leads to very little variation in the intensity of HCN.

The level populations of HCN were calculated in RADMC-3D using the large velocity gradient (LVG) approximation (Sobolev 1957) as implemented by Shetty et al. (2011). We use the collisional rate data for HCN provided by Leiden Atomic and Molecular Database (Schöier et al. 2005; Faure et al. 2007; Dumouchel, Faure & Lique 2010). In this study, we use the version of the HCN line data without hyperfine structure, and we include excitation from two collisional partners, H_2 and electrons. The radiative transfer is performed along the z-axis of the grid (perpendicular to the axis of the cloud–cloud collision), such that the rays are directed from negative to positive z.

3 OVERVIEW OF THE CLOUD-CLOUD COLLISION SIMULATIONS

We present four cloud–cloud collision simulations, with each investigating a different collision velocity, as outlined in Section 2.2. In Fig. 2, we show the evolution of the 3.75 km s^{-1} simulation from its initial conditions to give the reader a better understanding of how our clouds evolve. Fig. 2 shows that even though the simulations begin from unrealistic spheres, the simulations evolve over time to form dense filamentary structures, consistent with the chaotic environment familiar from both previous colliding flow models and from observational studies of molecular clouds. As the clouds meet, the two supersonic colliding flows cause a shocked layer at the point of impact creating a layer of dense gas. This process repeats as more of the inflowing gas from the opposing edges of the clouds fall into the shocked dense region.

All simulations are evolved to a point ∼1–3 Myr after the formation of the first sink particle, which we will denote as t_{SF} – the time of 'star formation'. In each of simulations, t_{SF} occurs at roughly 15, 11, 9, and 12 Myr for the 1.875, 3.75, 7.5, and 15 km s^{-1} initial bulk velocities, respectively.

In Fig. 3, we plot the evolution of the mass above different density thresholds (n_{thr}) as a function of time. We see that a higher collision velocity between the two clouds decreases the time taken to form gas above $n_{thr} \sim 10^4$ cm^{-3}. However, this trend does not continue as we move to higher n_{thr}: the faster flow of 15 km s^{-1} has a clear difficulty in forming gas with density above 10^6 cm^{-3}, and indeed actively seems to lose gas above $n_{thr} \sim 10^4$ cm^{-3} at times between ∼4–8 Myr. This implies that much of the dense gas that is initially created in the 15 km s^{-1} simulation is not self-gravitating, and either re-expands once the confining flow has finished, or is shredded by further interactions with surrounding flows. Only at late times (beyond around 8 Myr), once some of the collisional kinetic energy has been dissipated, there are gravitationally bound regions able to form providing an increase in the dense gas fractions. The dip and rise in the $n_{thr} = 10^3$ cm^{-3} line indicates that this occurs at initially quite low densities (and thus large scales).

Using Fig. 3, we can see that by the point at which we terminate the simulation (as presented in the graph's timeline), somewhere between 0.5–3.6 per cent of the total cloud mass sits above a density of 10^4 cm^{-3} and 0.04–0.2 per cent of the total cloud mass above a density of 10^6 cm^{-3}. The simulations have therefore evolved far enough for us to proceed with the analysis of the HCN emission with RADMC-3D, as they contain gas at densities commonly associated with prestellar cores, and starting to form sink particles.

Before looking at the HCN emission, we first examine how much 'dense' gas is actually present in the simulations. We show in Fig. 4

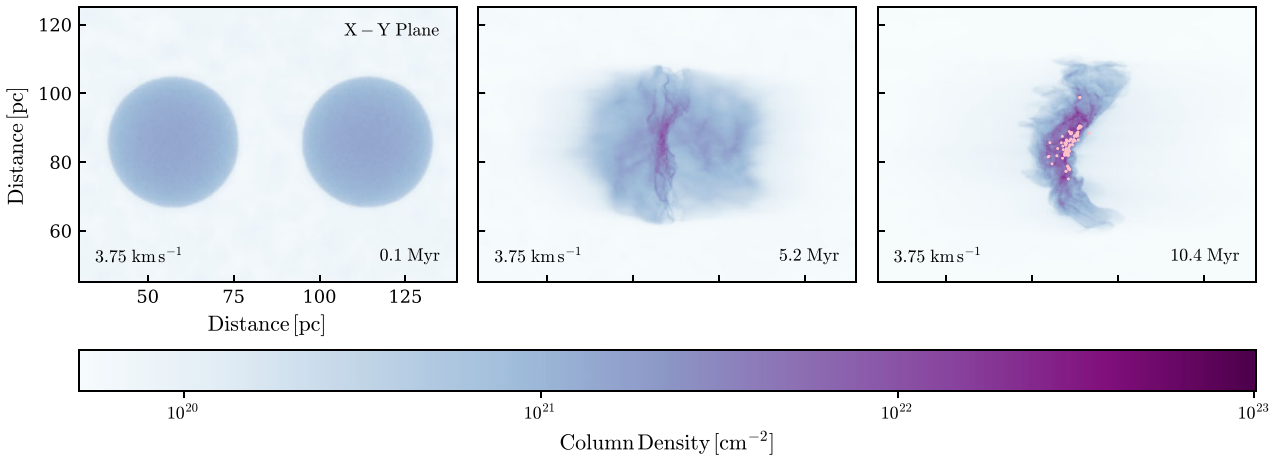

Figure 2. Column density of the 3.75 km s^{-1} simulation at three different times, one at the start of our simulation, and the other two at 5.2 Myr intervals. The sink particle locations are also included in any image that possess sink particles which are represented as pink points.

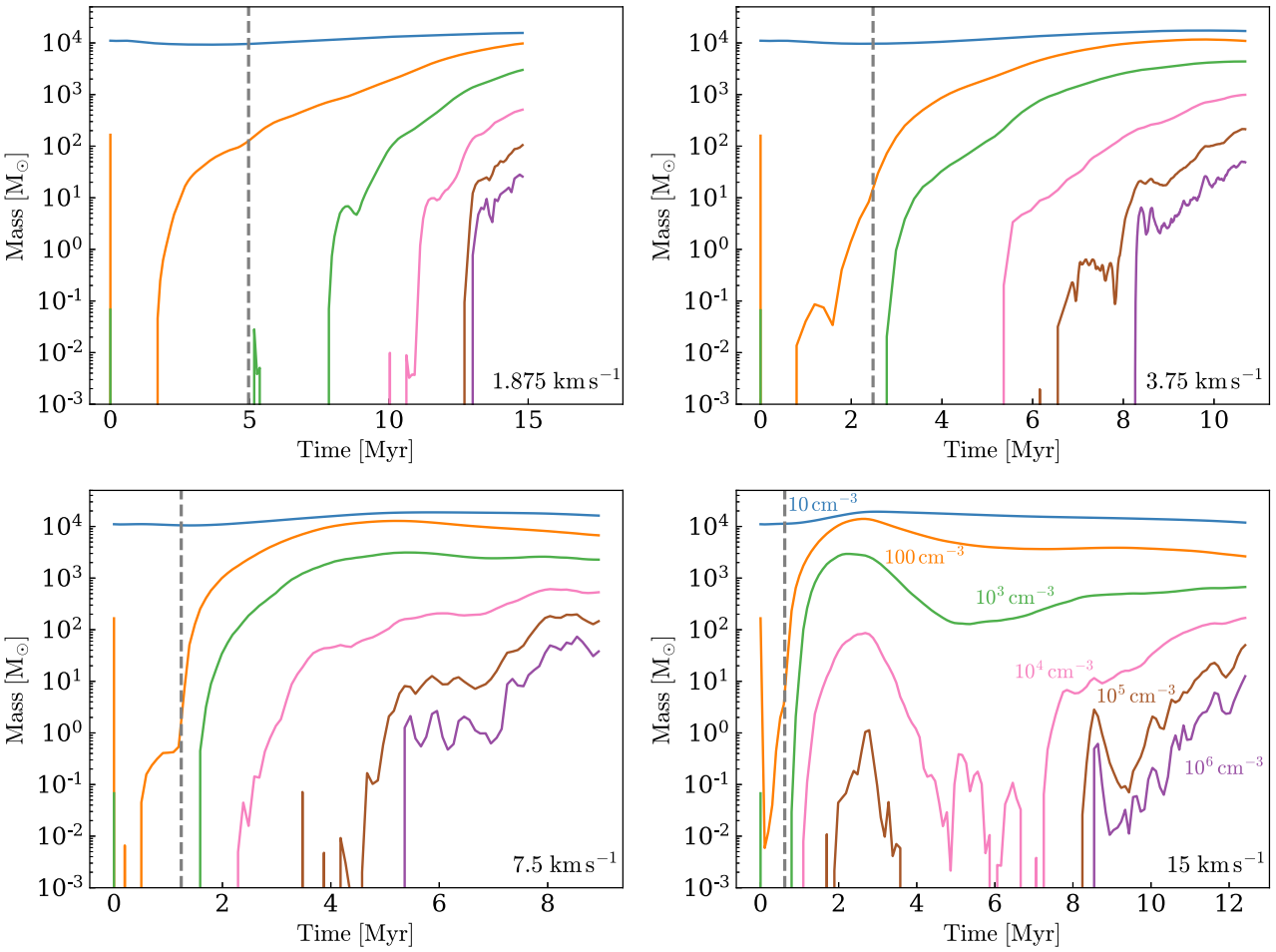

Figure 3. Evolution of mass of the gas within the simulations that lies above a given density threshold, which is labelled on the final plot. Each plot shows the evolution of mass with different initial velocities. From left to right, we have initial velocities of 1.875 , 3.75 , 7.5, 15 km s^{-1}. Note that the grey vertical line denotes the approximate time at which the edge of both clouds come into contact.

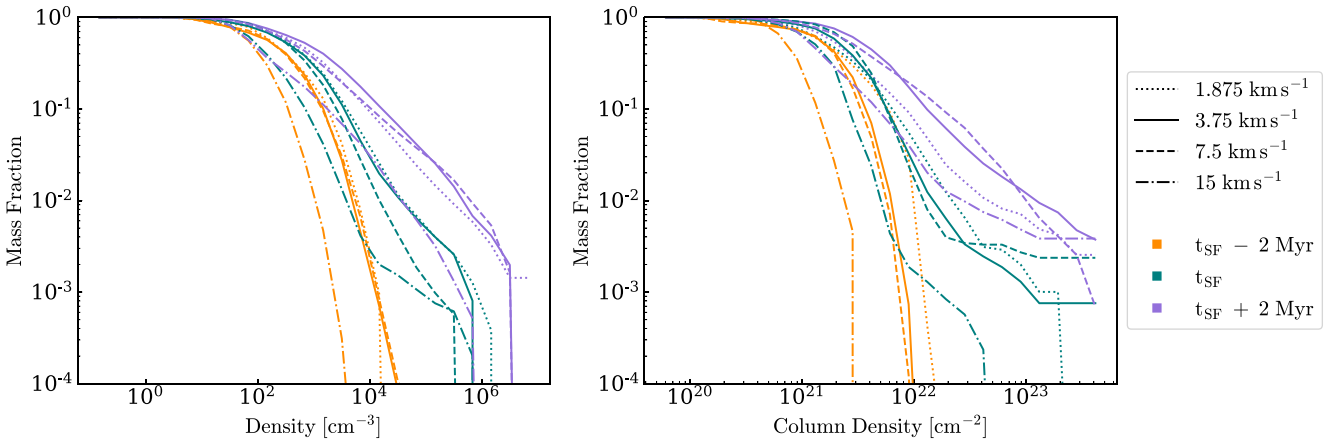

Figure 4. Comparison of the normalized mass-weighted complementary cumulative distribution function (CCDF) for both density and column density for all four simulations at the three different output times. Note that we vary our line-styles based on the initial cloud velocities at the start of our simulations, and vary the colour based on the three different output times.

a normalized mass-weighted complementary cumulative distribution function (CCDF) for both density and column density for all twelve simulations. It is clear from Fig. 4 that the amount of high-density gas is more sensitive to when we look at the simulation than the collision velocity of the flow. Again, we see the same behaviour as in Fig. 3, in that the fastest flow actually has (typically) the least amount of dense gas. With the other flows, the situation is more complicated. It is also clear that as stated previously, there is only a very small

Table 1. A brief overview of all twelve cases that were post-processed through RADMC-3D.

ID	Initial velocity [km s^{-1}]	Time [Myr]	Mass [M$_\odot$]	HCN luminosity [K km s^{-1} pc^2]	$W_{\rm HCN}^{\rm mean}$ [K km s^{-1}]	Fraction of mass above 2.85×10^3 cm^{-3} [per cent]	Fraction of mass above 3×10^4 cm^{-3} [per cent]
A	1.875	12.22	2176.49	15.92	0.16	9.37	0.02
B	1.875	13.31	2929.12	34.67	0.35	19.36	1.78
C	1.875	14.51	3590.91	55.43	0.55	27.11	5.69
D	3.75	6.46	2026.82	8.28	0.08	6.65	0.03
E	3.75	8.35	3153.03	42.40	0.42	18.18	1.52
F	3.75	10.69	4129.07	109.79	1.09	35.23	8.69
G	7.5	3.48	1971.21	2.93	0.03	6.61	0.03
H	7.5	5.47	3414.21	45.39	0.45	13.71	0.69
I	7.5	8.04	4380.66	118.16	1.18	25.28	6.92
J	15	5.07	1817.20	2.14	0.02	0.19	0.00
K	15	8.54	2636.88	15.15	0.15	2.82	0.17
L	15	11.60	2867.27	24.60	0.25	9.35	1.70

percentage of a molecular cloud's mass that goes into these high volumetric densities and column densities.

To investigate how the HCN emission varies with time, we perform a RT analysis at three different times in each simulation. The first time is taken to be $t_{\rm SF}$, and then we take two further times, roughly $\sim$2 Myr before and after $t_{\rm SF}$. In total this provides twelve different RT simulations of the HCN emission arising from a region of gas 10 pc on a side. These regions have fully consistent density, velocity, and magnetic fields, and have thermodynamics set by our detailed treatment of the heating and cooling in molecular clouds. The details of these regions are tabulated in Table 1, and in Fig. 5 we show the column density maps of each of the twelve cases that are used as the initial conditions for our post-processing with RADMC-3D.

4 HCN EMISSION FROM OUR CLOUDS

4.1 The density regime probed by HCN emission

To get a better sense of the formation of the HCN in our simulations, we present a HCN column density in Fig. 6 that is from the resulting application of equation (4) to our CO data in our simulation to generate our HCN abundances combined with Fig. 5.

Using the post-processed HCN abundances generated from AREPO, we create PPV cubes of the HCN ($J = 1 \rightarrow 0$) line emission using RADMC-3D for all twelve regions (three different times for each of our four simulations). All RADMC-3D simulations track the spectrum between -3 to 3 km s^{-1} in 0.02 km s^{-1} increments; this is sufficient to completely cover the range of velocities along the z direction in each of our 10 pc boxes, while allowing us to model the thermal line-width with around ten points.

From these PPV cubes, we create velocity-integrated intensity maps of HCN, which can be seen in Fig. 7. The contribution of each column density of gas has on the HCN emission can be seen in Fig. 8, and we see that as the column density increases the intensity of HCN emission also increases. It appears that HCN is above the observationally detectable limits of $\sim$0.1 K km s^{-1} only above a column density of $\sim 3 \times 10^{21}$ cm^{-2}, which is roughly an order of magnitude higher than our lower threshold on the CO to HCN conversion in Fig. 1. A similar behaviour in the HCN emission is reported by Pety et al. (2017), Kauffmann et al. (2017), and Barnes et al. (2020) who find $\sim$50 per cent emission stemming from column densities below 9.7×10^{21}, 1.2×10^{22}, and 2.1×10^{22} cm^{-2}, respectively.

The inclusion of sink particles in our figures allows us to clearly demonstrate that the regions of active star formation are associated with bright HCN emission. However, upon looking at cases C and F (see Table 1), we also see sink particles without any HCN emission demonstrating that star forming clouds can evolve rapidly: stars can be ejected from their natal environments, and young clusters may also consume the available gas on the local free-fall time. Note that there is no feedback from the sink particles in our simulations.

The main goal of this paper is to determine the density regime probed by HCN. We achieve this by manipulating the HCN abundance that goes into RADMC-3D. By artificially setting the HCN abundance in cells with a density below a certain threshold density, $n_{\rm thr}$, to zero in our RADMC-3D input cubes, and then performing the RT for the HCN line, we can determine the amount of HCN emission arising from gas with $n > n_{\rm thr}$. If we repeat this process, systemically varying $n_{\rm thr}$ from 10^2 to 10^6 cm^{-3}, we can work out the inverse cumulative fraction of HCN emission with density for each cloud. This analysis is repeated for all twelve of the simulated regions studied in this paper. However, it is standard to determine the cumulative fraction of emission i.e. the amount of HCN emission arising from gas with $n < n_{\rm thr}$. Therefore to do this, we simply take one minus our inverse cumulative fraction of HCN.

The results of this process can be seen in Fig. 9, in which the fraction of emission is given by the ratio of the HCN luminosity produced by gas below a certain density threshold, $n_{\rm thr}$, to that in the case where no threshold is applied – i.e. the HCN abundance is unchanged from the value derived from equation (4). In Fig. 9, we see $\sim$50 per cent of HCN emission emanates from densities below $\sim$1–7 $\times$ 10^3 cm^{-3}, with the scatter depending on both the evolutionary stage of the cloud in the simulation, and the collision velocity (the former proving a slightly larger scatter). This result goes against many observational results that postulate that most of the emission stems from densities above 10^4 cm^{-3} such as Gao & Solomon (2004a), Krumholz & Tan (2007). However, our result agrees with the more recent observational studies such as Shirley (2015), Kauffmann et al. (2017), Pety et al. (2017), Harada et al. (2019), Tafalla et al. (2021).

We see a trend towards a higher fraction of emission coming from higher densities as the simulations evolve over time, as they are able to accumulate a higher fraction of dense gas (as shown in Fig. 3). Therefore, one could argue that we could reach a point where the emission from dense gas overwhelmingly dominates. However, we see both observationally and through simulations that the fraction of gas above 10^4 cm^{-3} is generally small (Kainulainen et al. 2009;

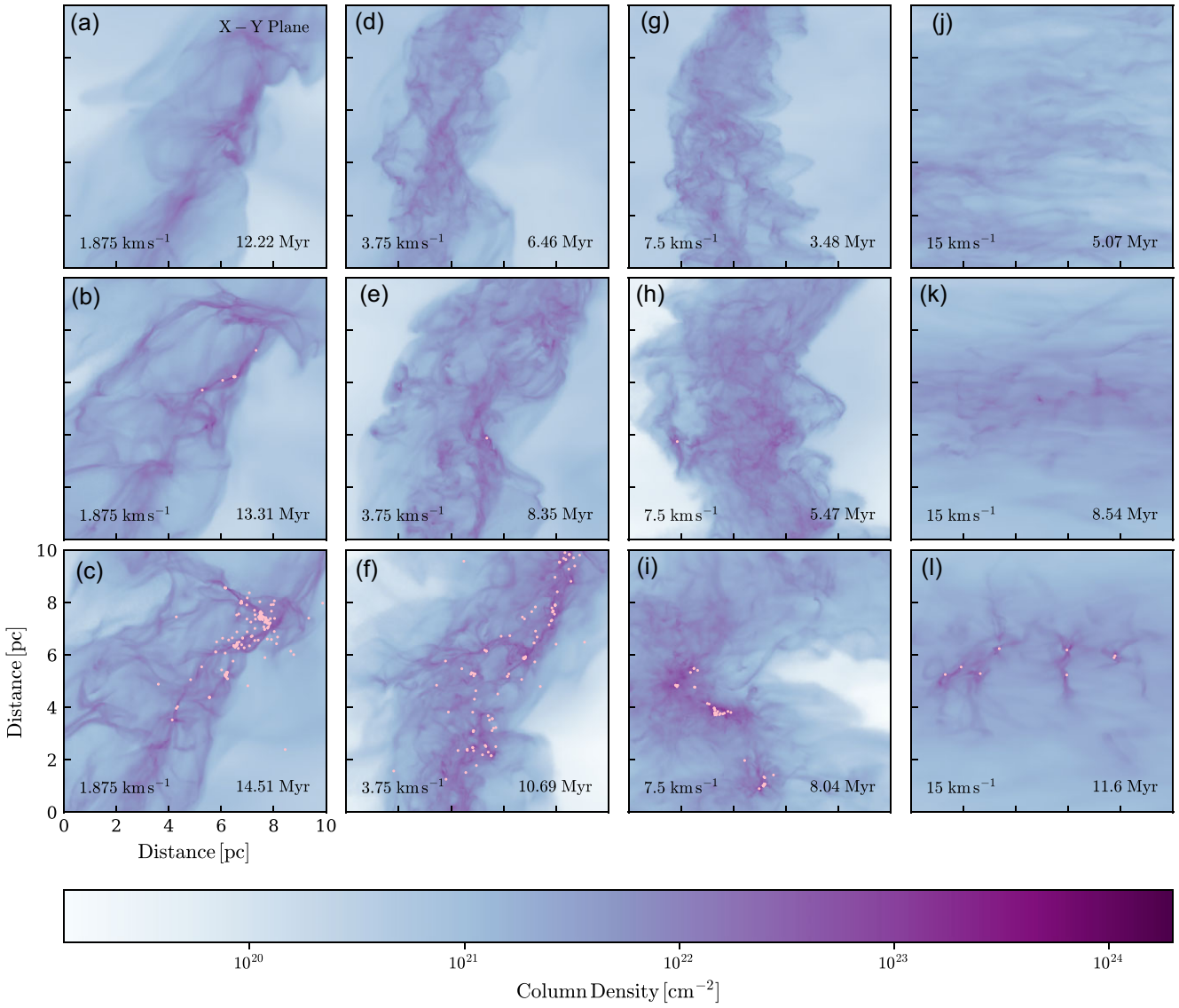

Figure 5. This grid of column densities shows the state of each simulation at the three points in their evolution where the RT is performed. The sink particle locations are also included in any image that possess sink particles, which are represented as pink points. Note that the alphabetical letters on each tile corresponds to the IDs in Table 1.

Lada, Lombardi & Alves 2010), at least outside the galactic centre (Longmore et al. 2013). It is therefore unclear if an environment with enough dense gas for the HCN emission to probe densities above 3×10^4 cm^{-3} is common in galaxies like the Milky Way, outside 'extreme' environments.

The idea that more dense gas equates to a higher threshold density for HCN emission actually breaks down as soon as we vary our cloud–cloud collision velocity. We see a trend of decreasing threshold density as we increase our initial cloud velocity, even though we generally see an increase in the mass of gas at higher densities as we increase the collision velocity (Fig. 3). The reason behind this is simply that the fraction of mass residing at densities above 10^3 cm^{-3} decreases as the initial cloud velocity of the simulation increases (see Table 1). As we will see below, it is around this density that is best traced by HCN (1–0) emission.

We can compare our results to those of Kauffmann et al. (2017) by adopting their definition of the 'characteristic density', $n_{\rm char}$, which is the density below which half of the total integrated intensity arises, i.e. $W_{\rm HCN}(n < n_{\rm thr})/W_{\rm HCN,Total} = 50$ per cent. From the data in Fig. 9, we determine that $n_{\rm char}$ is $2.85^{+4.25}_{-2.15} \times 10^3$ cm^{-3} for our suite of simulations (i.e. taking the mean from all our RT modelling). Our characteristic density lies in between those derived for Orion A – $0.87^{+1.24}_{-0.55} \times 10^3$ cm^{-3} (Kauffmann et al. 2017) – and W49–$3.4 \pm 2.8 \times 10^3$ cm^{-3} (Barnes et al. 2020).

A further comparison between our work and both Kauffmann et al. (2017) and Barnes et al. (2020) can be made by looking at the cumulative fraction of emission as a function of $A_{\rm V}$. Our column densities are derived by integrating along the z-direction in the RADMC-3D density cubes, to ensure that it is consistent with the 3D structure used in the RT (as opposed to deriving it straight from AREPO's more detailed Voronoi grid). The resulting column densities are then converted to $A_{\rm V}$ using equation (3). The cumulative total emission as a function of $A_{\rm V}$ is given in Fig. 10. We find that our results are closer to those found for Orion A by Kauffmann et al. (2017) than the results from W49 by Barnes et al. (2020). We discuss this further in Section 6.

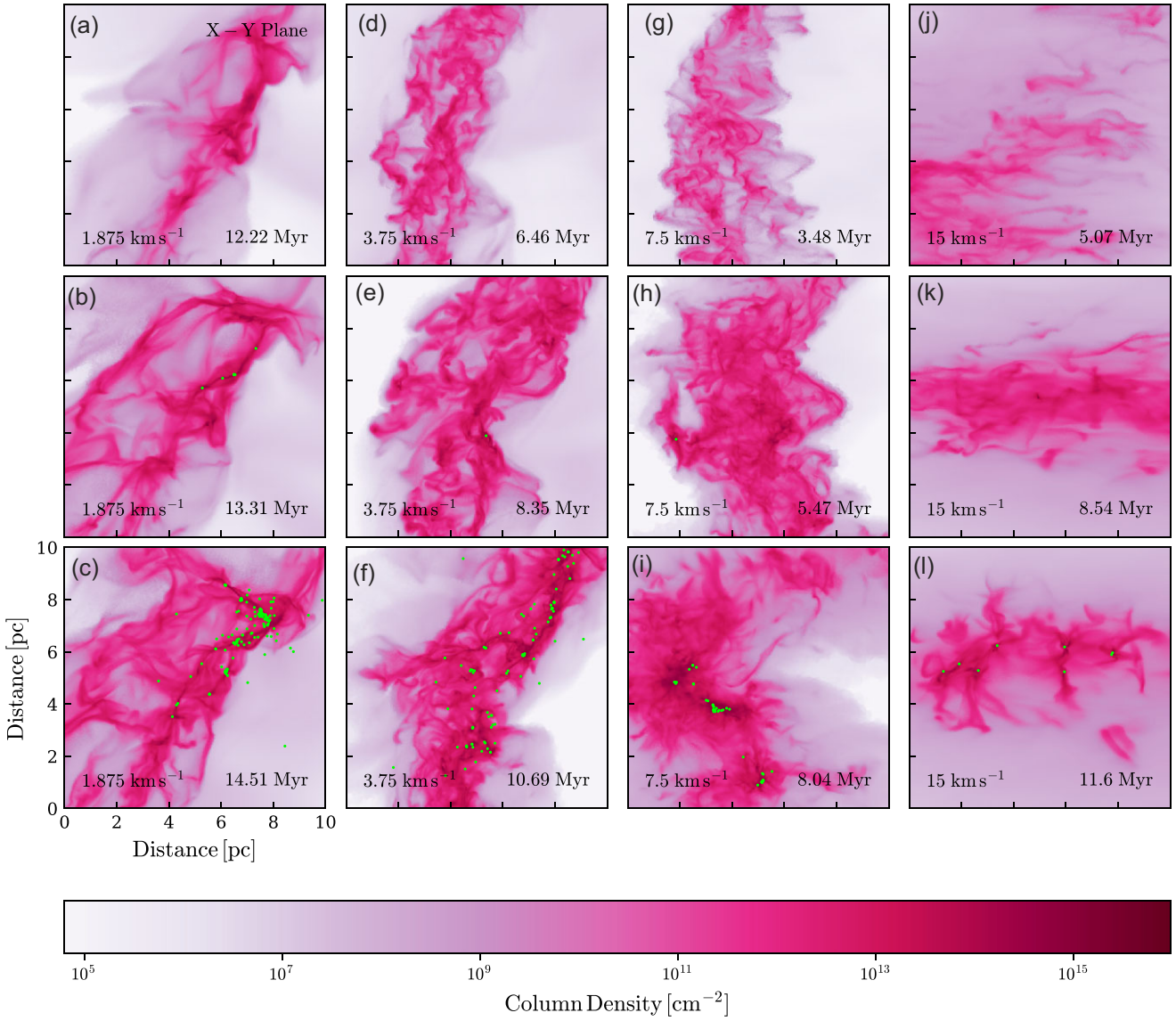

Figure 6. A grid of column densities of HCN for all simulations presented in the same format as in Fig. 5.

We can perform a similar analysis for the characteristic visual extinction, and define $A_{\rm V,\,char}$, where $A_{\rm V}$ contains half the total integrated intensity, or $W_{\rm HCN}(A_{\rm V} < A_{\rm V,\,thr})/W_{\rm HCN,\,Total} = 50$ per cent. From the data used to compile Fig. 10, we determine $A_{\rm V,\,char}$ to be $5.05^{+3.36}_{-3.07}$ mag.

While our value of $A_{\rm V,\,char}$ is consistent with that from Orion A, we can see from Fig. 10 that our simulations are not consistent with the data from W49. The fact that we see a different relation to Barnes et al. (2020) is not that surprising. First, their resolution is much cruder, nearly ∼3 pc, yet they report high-gas column densities. Given the low resolution, their high column density regions are likely probing much higher densities than in the Orion A observations, to compensate for the low densities that are likely mixed into emission within the beam. Second, W49 is a much denser region than those we study here, and so likely contains more gas at high densities than our clouds. Another big difference between W49 and the clouds modelled here is cloud mass. Our total available mass is 2×10^4 M$_\odot$, of which ∼10–20 per cent is in the region we study. On the other hand, the mass of the region Barnes et al. (2020) map in W49 is $\sim 2 \times 10^5$ M$_\odot$, and the mass of the entire W49 complex is larger still, $\sim 10^6$ M$_\odot$.

Finally, the observations of W49A focused around the star-forming region of W49A and not the entire W49 region. As noted by Pety et al. (2017), HCN is sensitive to far-UV radiation that is produced from star formation. Our ISRF with $G_0 = 1.7$ is hence not representative of the radiation field found in the massive star forming region of W49A. In contrast, we see a good comparison with the data from Kauffmann et al. (2017), where the spatial resolution is very similar to that in our study: roughly ∼0.02 pc in this work, compared to ∼0.05 pc in the case of the Orion A observations. Along with Kauffmann et al. (2017) and Barnes et al. (2020), we see that our data is also consistent to that of Pety et al. (2017).

Finally, we can follow the analysis in Kauffmann et al. (2017) by examining the emission efficiency ratio, $h_{\rm HCN} = W_{\rm HCN}/N_{\rm H_2}$. In Fig. 11, we see the normalized ratio of the integrated intensity to the column density [or $h_{\rm HCN}/h^{\rm max}_{\rm HCN}$] as a function of column density. We see a clear trend with all of our simulations in that they all peak at

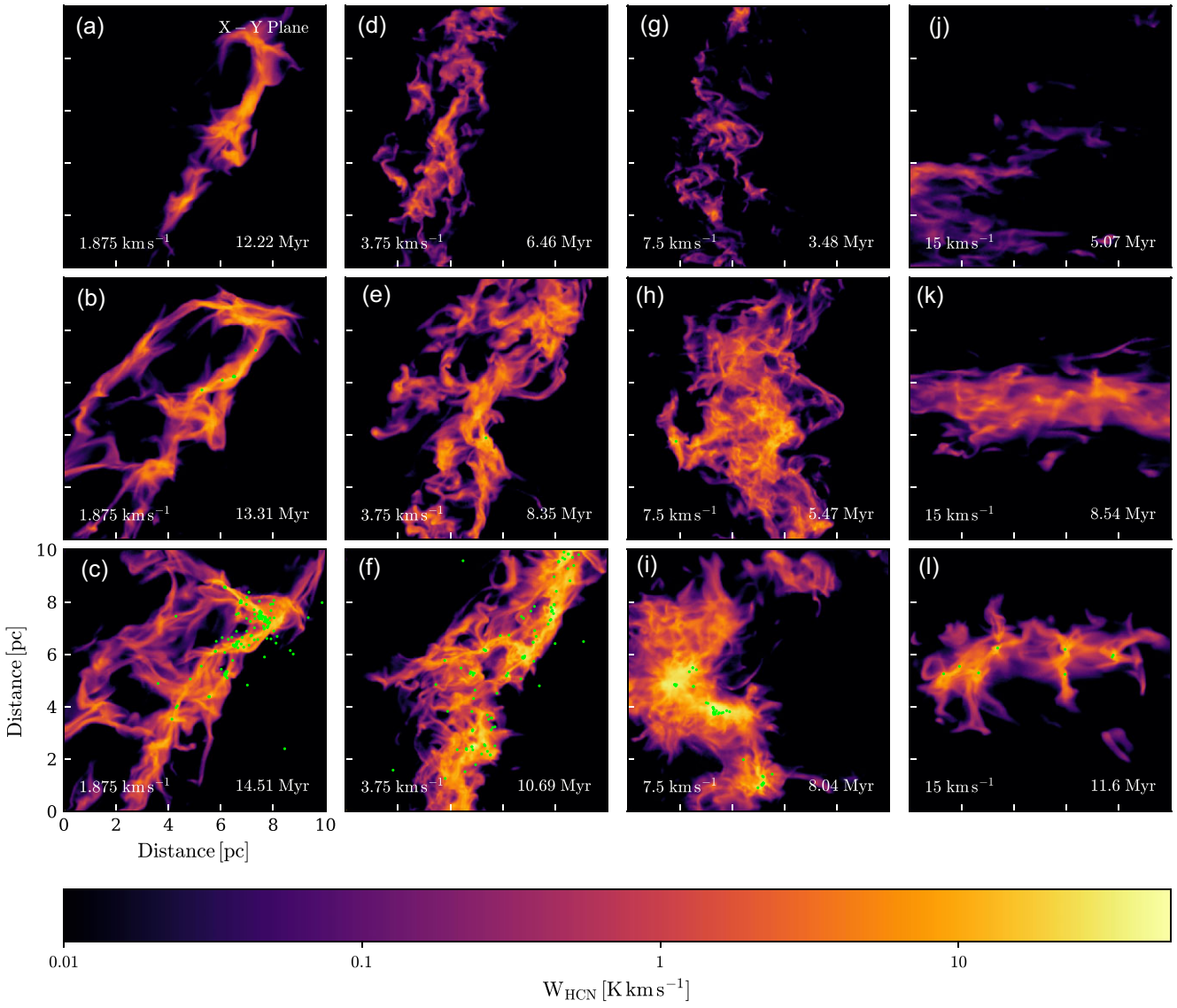

Figure 7. Maps of the velocity-integrated intensity in the $J = 1 \rightarrow 0$ line of HCN, $W_{\rm HCN}$, at the three simulation times and the four initial velocities that were used in Fig. 5. Note that the alphabetical letters on each tile corresponds to the IDs in Table 1.

around a column density of 10^{22} cm^{-2} which is roughly equivalent to $A_{\rm V} = 5$ mag, which is again comparable to our findings above.

4.2 Using HCN emission to determine the mass of 'dense' gas

HCN emission has been used as way of tracing 'dense' gas in molecular clouds, with a conversion factor of the form,

$$\alpha_{\rm HCN} = M_{\rm dg}/L_{\rm HCN}, \quad (5)$$

where $\alpha_{\rm HCN}$ is units of M$_\odot$ (K km s^{-1} pc^2)$^{-1}$. The typically adopted value is $\alpha_{\rm HCN} \sim 10\,{\rm M}_\odot\,({\rm K\,km\,s^{-1}\,pc^2})^{-1}$ (Gao & Solomon 2004b). As already discussed, there is some uncertainty as to what exactly 'dense' means here, with (somewhat confusingly) both definitions based on volume and column density being used in the literature, as well as uncertainty over the value of the density being used in each case. In this section, we explore both the column density ($\alpha^{A_{\rm V}}_{\rm HCN}$) and volume density ($\alpha^{n_{\rm thr}}_{\rm HCN}$) versions of this conversion factor.

We start our discussion by looking at the conversion factors based on column density, or in this case visual extinction, such as explored by Kauffmann et al. (2017), Evans et al. (2020), Barnes et al. (2020). For clarity we will define,

$$\alpha^{A_{\rm V}}_{\rm HCN} = M_{A_{\rm V}>8\,{\rm mag}}/L_{\rm HCN}, \quad (6)$$

where $M_{A_{\rm V}>,8\,{\rm mag}}$ is the mass residing above an $A_{\rm V} > 8$ mag, as given in Evans et al. (2020) and Barnes et al. (2020). This is in keeping with the result from Lada et al. (2010), Lada et al. (2012), who defined a 'threshold' surface density of 8 mag above which the vast majority of dense cores are found. Note however that Kauffmann et al. (2017) uses a visual extinction of 7 mag in their analysis.

In Fig. 12, we present the conversion factor, $\alpha^{A_{\rm V}}_{\rm HCN}$, as derived from our simulation data, adopting the definition given in equation (6). To mimic the effects of limited observational sensitivity, we only consider pixels of integrated emission – and thus the corresponding pixels in the column density ($A_{\rm V}$) maps – that would be detected with a signal to noise greater than 3 for an assumed uniform noise level of $\sigma = 0.1({\rm K\,km\,s^{-1}})$. For comparison, we also show the results in the noise-free case.

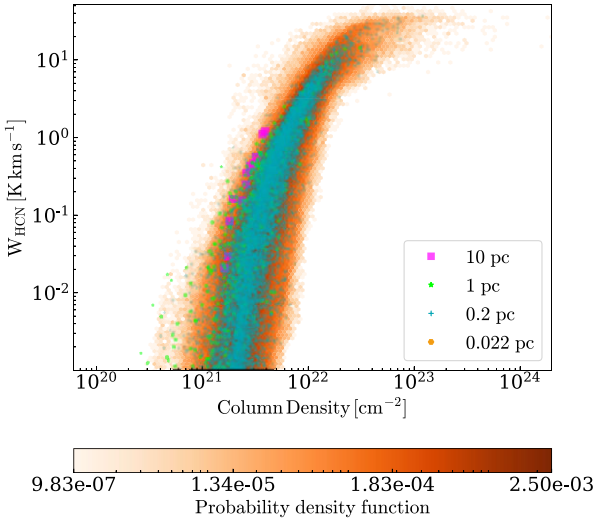

Figure 8. Velocity-integrated intensity in the $J = 1 \rightarrow 0$ line of HCN, W_{HCN}, plotted against the column density for all simulations collated into one figure. We also demonstrate what happens if we degrade the spatial resolution of the PPV cubes to 0.2, 1, or 10 pc.

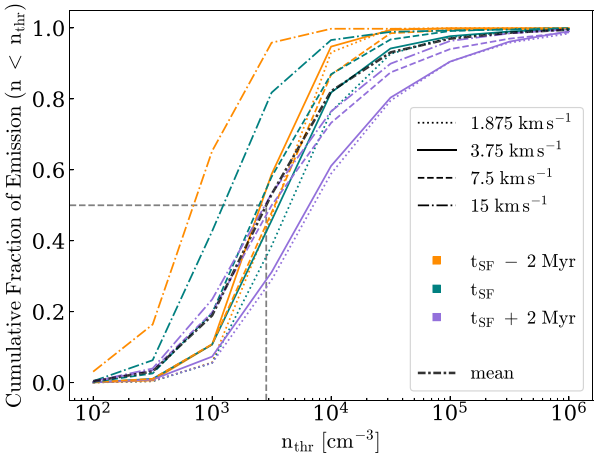

Figure 9. Cumulative fraction of emission of HCN plotted as a function of density for all four simulations at the three different output times. Note that we use the same stylistic format as Fig. 4. Also included is the mean cumulative fraction of emission (densely dash–dotted black line), plotted as a function of density. The dashed grey line indicates the mean value of the characteristic density, $n_{char} = 2.9 \times 10^3$ cm^{-3}.

It is clear from Fig. 12 that there is a broad scatter in the values of $\alpha_{HCN}^{A_V}$ derived from our simulations, and that the values are largely unaffected by the choice of σ. We therefore ignore the effect of σ on our analysis. The mean value of $\alpha_{HCN}^{A_V}$ from our suite of simulations is $\alpha_{HCN}^{A_V} = 6.79\,M_\odot\,(K\,km\,s^{-1}\,pc^2)^{-1}$. Although this is close to the value quoted in Gao & Solomon (2004b), the standard deviation is $3.79\,M_\odot\,(K\,km\,s^{-1}\,pc^2)^{-1}$, which is over half the mean value of $\alpha_{HCN}^{A_V}$.

We can demonstrate the effect of adopting an incorrect $\alpha_{HCN}^{A_V}$ by determining the mass we would expect to get above an A_V of 8 mag using equation (6), and comparing to the actual mass in our simulations that lies above an A_V of 8 mag. We show the results of this analysis in Fig. 13. We see that for a low amount of dense gas – around $10\,M_\odot$, such as one might find in a handful of prestellar cores – the standard α_{HCN} relation overestimates the amount of dense gas

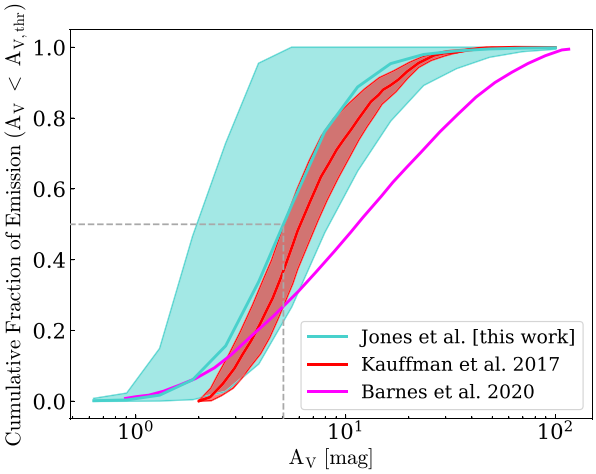

Figure 10. Cumulative emission of HCN plotted as a function of A_V with the mean, minimum, and maximum cumulative emission from all twelve simulations. We include the cumulative emission of HCN from Kauffmann et al. (2017) and Barnes et al. (2020) for comparison.

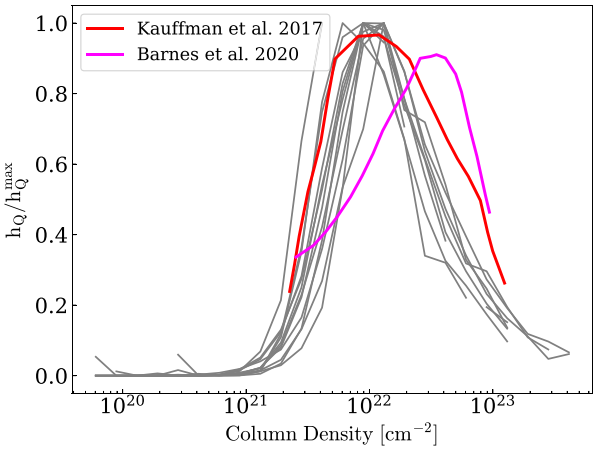

Figure 11. A normalized ratio of the integrated intensity to the column density, h_{HCN}/h_{HCN}^{max}, where $h_{HCN} = W_{HCN}/N_{H_2}$, as a function of column density. All of our twelve simulations are grey for clarity. We include Kauffmann et al. (2017) and Barnes et al. (2020) for comparison.

present by up to an order of magnitude. However, once the clouds contain $M_{A_V>8\,mag} > 100\,M_\odot$, the standard $\alpha_{HCN}^{A_V}$ actually predicts the amount of dense gas very well. This suggests that provided one is already looking at well-evolved, and active star-forming regions, the true scatter in $\alpha_{HCN}^{A_V}$ will not significantly affect the predicted mass. However, for regions of low star formation (i.e. early in a cloud's star-forming evolution), one could significantly overpredict the amount of dense gas present.

We can also do the same analysis using our value of $A_{V,char} = 5.05$ mag that we we derived above, instead of A_V of 8 mag in equation (6). Here, we get a mean value of $\alpha_{HCN}^{A_V} = 19.46\,M_\odot\,(K\,km\,s^{-1}\,pc^2)^{-1}$. We can use this value of $\alpha_{HCN}^{A_V}$ to repeat the analysis we just performed with A_V of 8 mag for our $A_{V,char}$ of 5.05 mag, which can be seen in Fig. 13. We see that using an $A_{V,char}$ of 5.05 mag is a much more reliable estimate of mass across all stages of our suite of simulations.

We can now perform a similar analysis for the conversion factor between HCN emission and gas above a threshold volume density, $\alpha_{HCN}^{n_{thr}}$. As described in Gao & Solomon (2004a, see also Barnes et al.

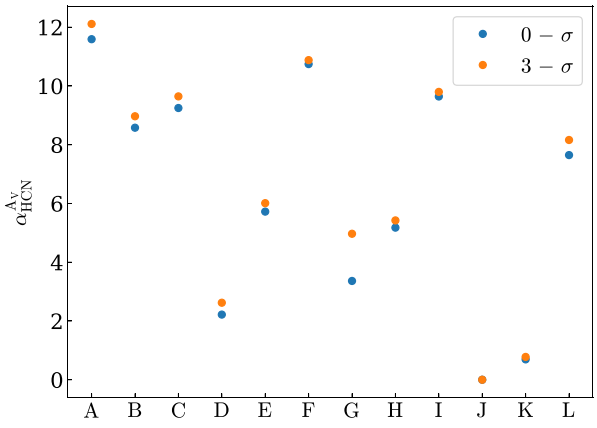

Figure 12. The conversion factor, $\alpha_{HCN}^{A_V}$, in each of the twelve cases considered in this paper. Note that the conversion factors here correspond to the use of an A_V above 8 mag as seen in equation (6). Here, the ID's of each simulation corresponding to Table 1 are given. The orange points show the values we obtain if we restrict the calculation to pixels, where HCN is detected with signal to noise > 3 for an assumed noise level $\sigma = 0.1(\mathrm{K\,km\,s^{-1}})$. The blue points show the result in the ideal noise-free case. We see that in most cases, the inclusion of a realistic amount of noise makes very little difference to the derived value of $\alpha_{HCN}^{A_V}$.

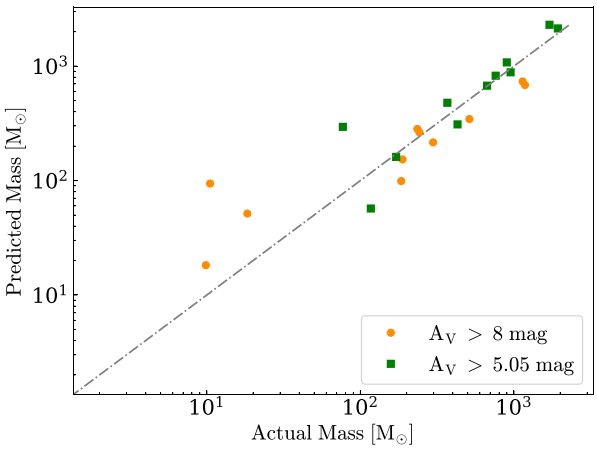

Figure 13. A plot of predicted mass for all simulations using a re-arranged version of equation (6) where $\alpha_{HCN} = 6.79\,M_\odot\,(\mathrm{K\,km\,s^{-1}\,pc^2})^{-1}$ for $A_V > 8$ mag compared to the actual mass calculated within regions of $A_V > 8$ mag and $\alpha_{HCN} = 19.46\,M_\odot\,(\mathrm{K\,km\,s^{-1}\,pc^2})^{-1}$ for $A_V > 5.05$ mag compared to the actual mass calculated within regions of $A_V > 5.05$ mag. The dashed line denotes the point at which the predicted mass is equivalent to the actual mass.

2020), the mass above the threshold density can be given by,

$$M_{n>n_{thr}}^{sum} \approx 2.1 \frac{n_{thr}^{0.5}}{T_B} L_{HCN}, \quad (7)$$

where T_B is the intrinsic HCN line brightness temperatures and n_{thr} is our density threshold. The factor of $2.1 n_{thr}^{0.5}/T_B$ can hence be identified with the volume density based conversion factor, $\alpha_{HCN}^{n_{thr}}$.

The intrinsic brightness temperature for equation (7) would simply be the peak main beam temperature of the spectra, provided that we are dealing with extended sources (i.e. the source is filling the beam) like Barnes et al. 2020. However, if we take our box to be the beam, we clearly have a case where the source is much smaller than the telescope beam. Indeed, we see this in Fig. 14 where the main beam

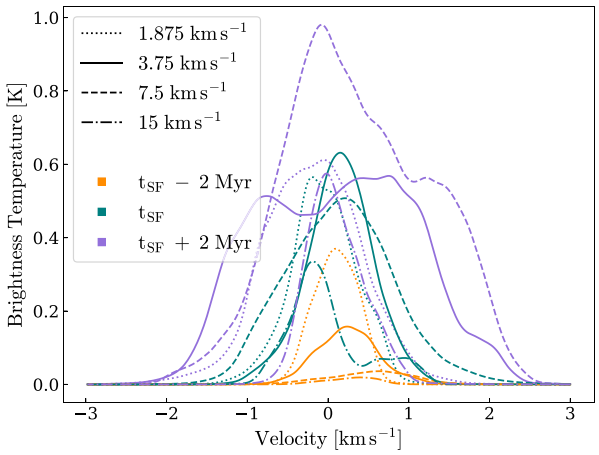

Figure 14. HCN (1–0) spectra of all simulations. The lines styles and colours are the same as Fig. 4. We take the mean emission of our entire 10 pc box. This is repeated for all velocity channels for all simulations to produce the observed spectra.

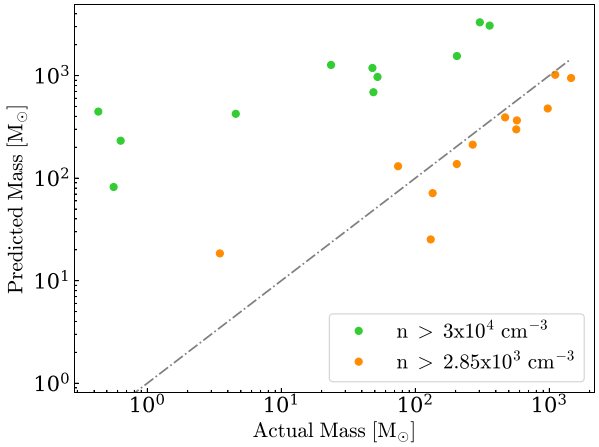

Figure 15. A plot of predicted mass for all simulations using equation (7) for our density threshold of $2.85 \times 10^3\,\mathrm{cm^{-3}}$ and Gao & Solomon (2004a) density threshold of $3 \times 10^4\,\mathrm{cm^{-3}}$ compared to the actual mass calculated above these two density thresholds. The dashed line denotes the point at which the predicted mass is equivalent to the actual mass.

temperatures are at least an order of magnitude lower than those seen in Barnes et al. 2020. In this case, we would have to take into account the solid angle of the source convolved with the diameter (FWHM) of the telescope Gaussian beam θ_{MB} (see section 4.2 in Gao & Solomon 2004a). Since all the observational studies have a different set-up, we instead use our pixel size as the main beam size and therefore our intrinsic brightness temperature is simply our pixel brightness temperature.

From our simulations, we find T_B to vary between 6 and 14 K, with a mean of roughly 13 K. We now consider two values for n_{thr}: first, we input the density that is most commonly adopted in the literature (Gao & Solomon 2004a) of $3 \times 10^4\,\mathrm{cm^{-3}}$; and second we input our characteristic density of $2.85 \times 10^3\,\mathrm{cm^{-3}}$ that we established from our simulations in Section 4.1. This yields a conversion factor of $\alpha_{HCN}^{n_{thr}} = 8.62\,M_\odot\,(\mathrm{K\,km\,s^{-1}\,pc^2})^{-1}$ for $n > 2.85 \times 10^3\,\mathrm{cm^{-3}}$ and $\alpha_{HCN}^{n_{thr}} = 27.98\,M_\odot\,(\mathrm{K\,km\,s^{-1}\,pc^2})^{-1}$ for $n > 3 \times 10^4\,\mathrm{cm^{-3}}$.

We see from Fig. 15 that our lower calculated density of $2.85 \times 10^3\,\mathrm{cm^{-3}}$ is able to reproduce the actual mass far better than $3 \times 10^4\,\mathrm{cm^{-3}}$. In contrast, the standard value of $n_{thr} = 3 \times 10^4\,\mathrm{cm^{-3}}$

Table 2. Summary of our findings of both the characteristic density and characteristic visual extinction traced by HCN emission. For comparison, we also quote the values from two recent observational studies.

Reference	$A_{\rm V,\,char}$ [mag]	$n_{\rm char}$ [$\times 10^3$ cm^{-3}]
Jones et al. [this paper]	$5.05^{+3.36}_{-3.07}$	$2.85^{+4.25}_{-2.15}$
Kauffmann et al. (2017)	$6.1^{+1.2}_{-1.0}$	$0.87^{+1.24}_{-0.55}$
Barnes et al. (2020)	11.9 ± 1.1	3.4 ± 2.8

consistently overpredicts the amount of mass above this density in our simulations by at least an order of magnitude; in one extreme case it predicts 59.9 $M_\odot$ above 3×10^4 cm^{-3} even though the simulation contained no mass above this density.

4.3 The effect of optical depth on the HCN emission

We can take advantage of the fact that RADMC-3D can produce optical depth maps of our simulations to explore the effect that the optical depth has on the emission of HCN. Selecting this option in RADMC-3D generates a PPV cube of optical depths (we will use $\tau_{\rm HCN}$ for the remainder of the paper) instead of emission. We can then use these $\tau_{\rm HCN}$ PPV cubes to find out if the use of $n_{\rm H} \gtrsim 6 \times 10^4/\tau$ cm^{-3} by the likes of Gao & Solomon 2004a and Krumholz & Tan 2007 is justifiable since we can use our $\tau_{\rm HCN}$ to predict an effective density and compare it to our effective density from Table 2. Note that we restrict our analysis to the $t_{\rm SF} + 2$ Myr snapshots as this is where we find the most dense gas (e.g. Fig 4).

We can create maps of the mean optical depth along a line of sight by defining,

$$\langle \tau_{\rm HCN} \rangle = \frac{\sum_i \tau_i \times T_i}{\sum_i T_i}, \quad (8)$$

where i denotes the index of the PPV cube along the velocity axis. The maps of mean optical depth for all four initial velocities are shown in Fig. 16.

We see from Fig. 16 that $\langle \tau_{\rm HCN} \rangle$ is high, above 10, towards the bright regions of HCN emission that we see in Fig. 7, which are associated with column densities in excess of 10^{22} cm^{-2} (see Fig. 5). However, $\langle \tau_{\rm HCN} \rangle$ is substantially lower than this for most of the map. To get a better idea of the optical depths associated with the bulk of the emission, we show in Fig. 17 the fraction of emission of HCN as a function of $\tau_{\rm HCN}$. We see that the the peak fraction of emission occurs at around $\tau_{\rm HCN} = 1$ for all four simulations. However, from the cumulative distributions, we see that only between 33 per cent and 41 per cent of the emission emanates from $\tau_{\rm HCN} > 1$, as summarized in Table 3.

To give some indication of the variations of the optical depth with velocity (and thus along the line of sight), we also select a small region of 10×10 pixels within these simulations to compare the mean line spectra to the mean $\tau_{\rm HCN}$ line. These regions are focused on bright spots in the integrated HCN intensity, and are labelled alphabetically in Fig. 16. In contrast to the low optical depth seen for the bulk of the cloud, the majority of the emission in these 10×10 pixel regions stems from $\tau_{\rm HCN} > 1$; indeed, we find some 83–95 per cent of the emission is associated with $\tau_{\rm HCN} > 1$.

Our analysis shows that while the effective critical density of the HCN might be lowered towards bright, dense (and possibly pre-star-forming) cores, this is not the case for the bulk of the emission in a molecular cloud such as those we study here. We conclude that the low effective density for HCN in our study is the result of subthermal excitation from a large amount of low-density material, rather than a lowering of the critical density, such as suggested by Barnes et al. (2020) and Gao & Solomon (2004a).

5 THE RELATIONSHIP BETWEEN HCN/CO AND DENSE GAS

As well as using the brightness of the HCN (1–0) line, we can also use the ratio of the HCN (1–0) and CO (1–0) lines to constrain the distribution of gas volume densities in molecular clouds (e.g. Gao & Solomon 2004b, García-Burillo et al. 2012, Leroy et al. 2017, Gallagher et al. 2018). Because each line traces densities above their effective densities (for a clear definition of effective densities, see Shirley 2015), $n_{\rm eff}$, a change in the ratio of intensities between two lines with different $n_{\rm eff}$ can gauge changes in the estimated dense gas mass fraction (see, for example, Krumholz & Thompson 2007 and Leroy et al. 2017). This multiple line method improves the accuracy with which variations in the sub-beam density distribution are recovered, and so is well-suited for low resolution studies i.e. galactic-scale studies, which use high effective critical density lines that tend not to fill the beam.

Due to the high effective critical density of HCN, galactic-scale studies have begun using HCN (1–0) to CO (1–0) integrated intensity ratio to estimate the distribution of gas volume density (e.g. Leroy et al. 2017, Gallagher et al. 2018, Querejeta et al. 2019). We therefore investigate how the HCN (1–0)/CO (1–0) integrated intensity ratio varies as a function of CO (2–1) line emission which is used as a proxy for surface density. We use the same RT code, RADMC-3D that we use for our HCN analysis. For both CO (1–0) and (2–1) lines, we use ortho- and para- H_2 as collisional partners along with the collisional rates provided by Leiden Atomic and Molecular Database (Jankowski & Szalewicz 2005; Schöier et al. 2005; Yang et al. 2010). When calculating the level populations of the CO, we assume that the gas has an H_2 ortho-to-para ratio of 3:1.

For this section, we create twelve PPV cubes for all three lines (HCN (1–0), CO (1–0), and CO (2–1)) and for all twelve cases characterized by Table 1. We create three additional resolutions for our analysis by degrading all twelve PPV cubes to 0.2, 1, and 10 pc, respectively. The resulting variation in the resolution can be seen in Fig. 8. A cut-off of 0.001 K km s^{-1} is placed on the velocity-integrated intensity of all three lines to limit our analysis to lines of sight, where the abundances are more certain.

We present our HCN/CO integrated intensity ratio against $W_{\rm CO\,(2-1)}$ in Fig. 18, which despite the scatter shows a clear correlation between $W_{\rm HCN}/W_{\rm CO}$ and $W_{\rm CO\,(2-1)}$. We see that the relation between these observables becomes progressively more linear as the resolution decreases. To compare with Gallagher et al. (2018), we present here a the results from a linear regression fit to the data in Fig. 18, assuming a power-law relationship between $W_{\rm HCN}/W_{\rm CO}$ and $W_{\rm CO\,(2-1)}$; the gradient of fit for all four resolutions is given in Table 4. We see that as the resolution decreases (i.e. the pixel area increases) the gradient of fit also decreases (see Table 4). Although the trend is consistent with the Gallagher et al. (2018) study, who find a similar relationship between these quantities with a gradient of between 0.55 to 0.81 for resolutions in the range 650–2770 pc, the fact that the slope changes so much with resolution for the same underlying data, implies there is no real physical justification for a linear relationship between these variables. At very high resolution, that is, when the beam (each pixel) is fully filled with emission, we find a much steeper relationship than that seen in the unresolved, galactic-scale observations. Once again, this suggests that one needs to be

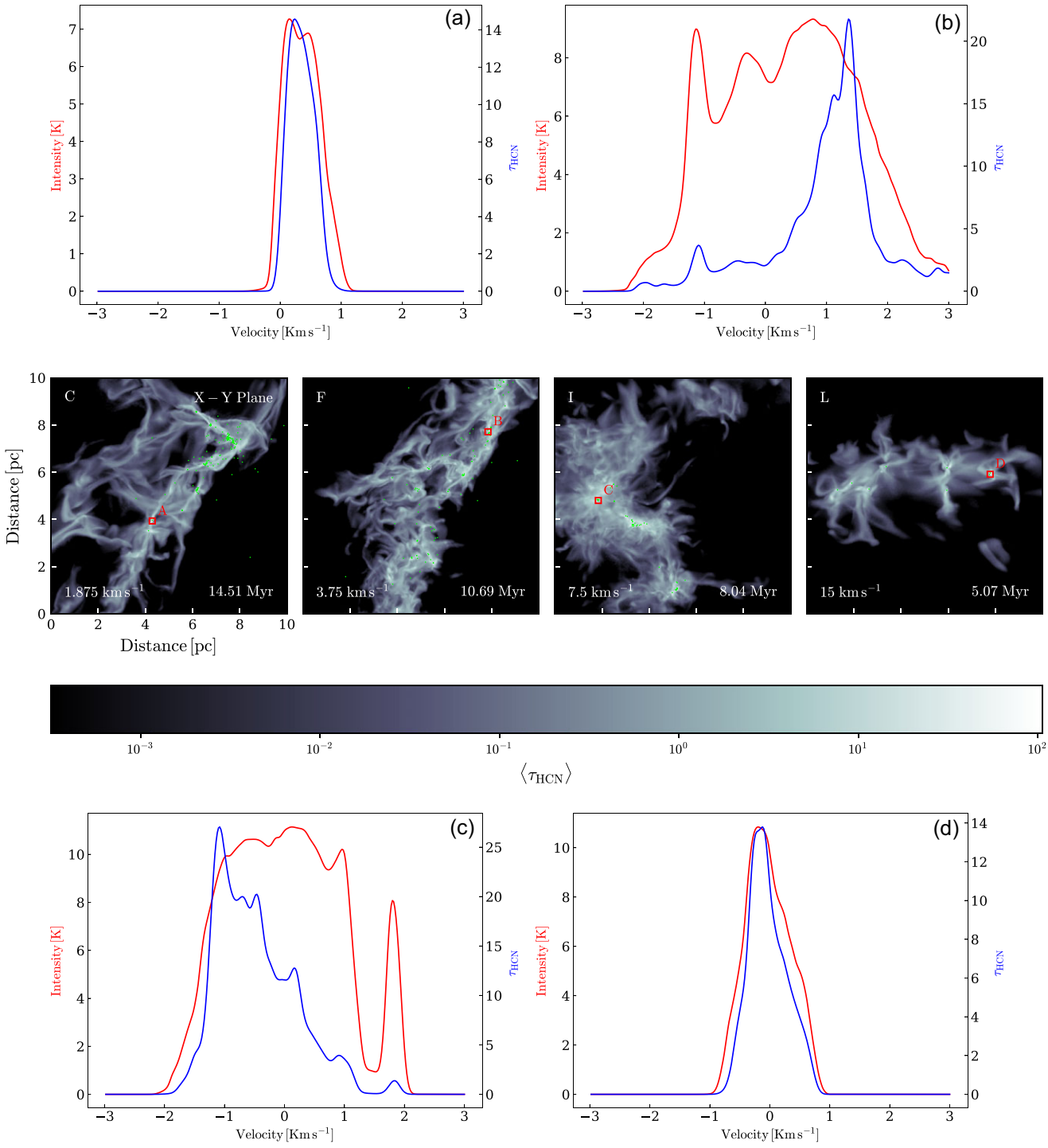

Figure 16. Emission-weighted integrated optical depth maps of the four initial velocities, all at the later simulation time surrounded by four line spectra and optical depths of selected regions labelled alphabetically (in red) on the optical depth maps. These regions are chosen with the peak optical depth as the centre of a square region with a size of 10 pixels, taking the mean emission and the mean optical depth of these square regions, and repeating through each velocity channel to produce the resulting four line profile plots.

extremely careful when interpreting data of this sort from galactic-scale surveys.

Our cut-off point of 0.001 K km s^{-1} in the emission used to generate Fig. 18 is significantly lower than the ∼0.1 K km s^{-1} noise limit of observational surveys. We therefore repeat the analysis above but with a higher velocity-integrated intensity cut-off of 0.1 K km s^{-1} on all three lines. For clarity, we plot the four different resolutions on four separate plots (see Fig. 19). With the higher cut-off, we lose the tail at low $W_{\rm CO\,(2-1)}$ that clearly has a very shallow gradient. We therefore would reasonably expect a steeper gradient for the higher cut-off analysis. However, using an ordinary least squares (OLS) fitting method, we get much shallower gradients than our

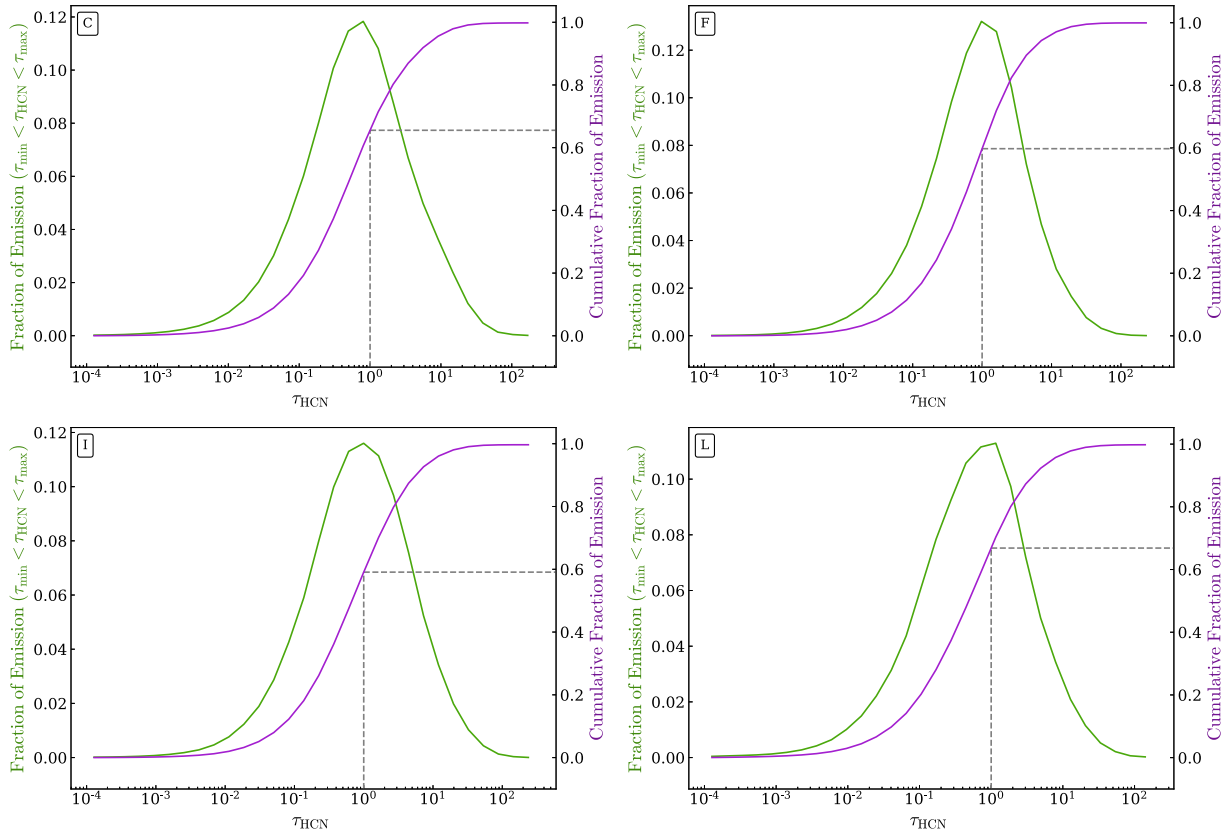

Figure 17. The fraction of HCN emission as function of optical depth (with accompanying cumulative fraction) for the four later stage simulations. The simulation IDs corresponds to those used in Table 1.

Table 3. A table of the percentage of cumulative fraction of emission emanating from $\tau_{HCN} > 1$ from Fig. 17.

ID	Percentage [per cent]
C	34.5
F	40.2
I	40.9
L	33.2

lower cut-off of 0.001 K km s^{-1} (see Table 5), since it is sensitive to the outliers from the main trend (the main ridge that you can see by eye). One could also argue that, observationally, there should be errors in both variables, and so OLS is not a statistically valid method for exploring a relation in this data. We therefore compare the OLS to a total least squares (TLS) fitting method that minimizes the orthogonal difference of both the dependent and independent variables to the predicted best-fitting model. Using TLS to fit our data, we recover a best fit gradient that follows a high-density ridge in the scatter. We now see much steeper gradients than what we saw for both OLS fitting of the cut-off of 0.001 K km s^{-1} and also 0.1 K km s^{-1}. We conclude here that the correlation in HCN/CO integrated intensity ratio against $W_{CO\,(2-1)}$ in previous studies might be in fact due to the resolution and not necessarily due to a physical correlation. Indeed, our RT results would suggest that the underlying correlation between W_{HCN}/W_{CO} and $W_{CO\,(2-1)}$ is significantly more complex.

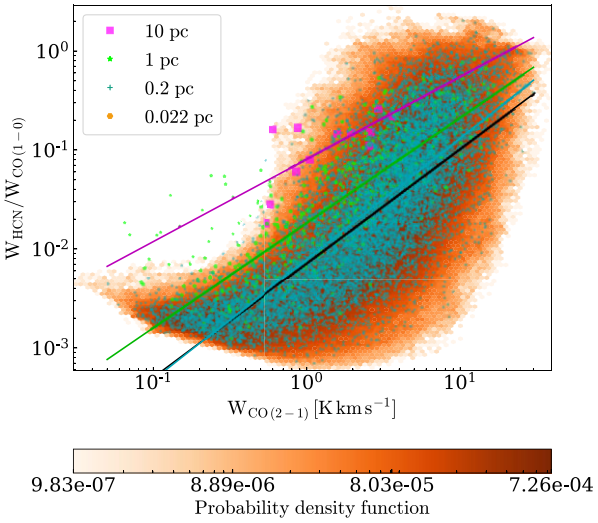

Figure 18. A plot of HCN/CO integrated intensity ratio against the velocity-integrated intensity of CO (2–1) at four different resolutions of 0.022, 0.2, 1, and 10 pc. Note that a cut-off of 0.001 K km s^{-1} is placed to simulate an observational cut-off due to noise.

6 DISCUSSION

Although our work, and those of recent observational and numerical studies (Kauffmann et al. 2017, Pety et al. 2017, Onus et al. 2018, Barnes et al. 2020 and Evans et al. 2020), suggests that HCN

Table 4. Summary of our results of comparison between HCN/CO (1–0) to $W_{CO\,(2-1)}$ for the 0.001 K km s^{-1}. Note that these gradients are obtained through ordinary least squares (OLS) fitting.

Resolution [pc]	Gradient of fit OLS
0.022	1.16
0.2	1.22
1	1.06
10	0.83

primarily traces lower density gas then previously assumed (Gao & Solomon 2004a; Krumholz & Tan 2007), there is an undeniable correlation between HCN emission and star formation (Gao & Solomon 2004a, b). More importantly, the correlation appears to be more linear than that between CO emission and star formation (e.g. Gao & Solomon 2004b). Hacar, Bosman & van Dishoeck (2020) has suggested that this correlation between HCN emission and star formation is due to the temperature dependence of the HCN to HNC abundance ratio, and that the ratio increases with temperature. In regions of star formation, where the interstellar radiation field is higher, we expect the gas to be hotter at the lower densities within the cloud (e.g. see Clark et al. 2019). The combination of higher HCN abundance and higher temperature is then proposed to boost the emission.

Although we do not include an explicitly temperature-dependent abundance in this paper, we can predict what the qualitative effect on our results would be. If our clouds were exposed to a higher degree of ambient star formation, the gas at low densities would be hotter, and

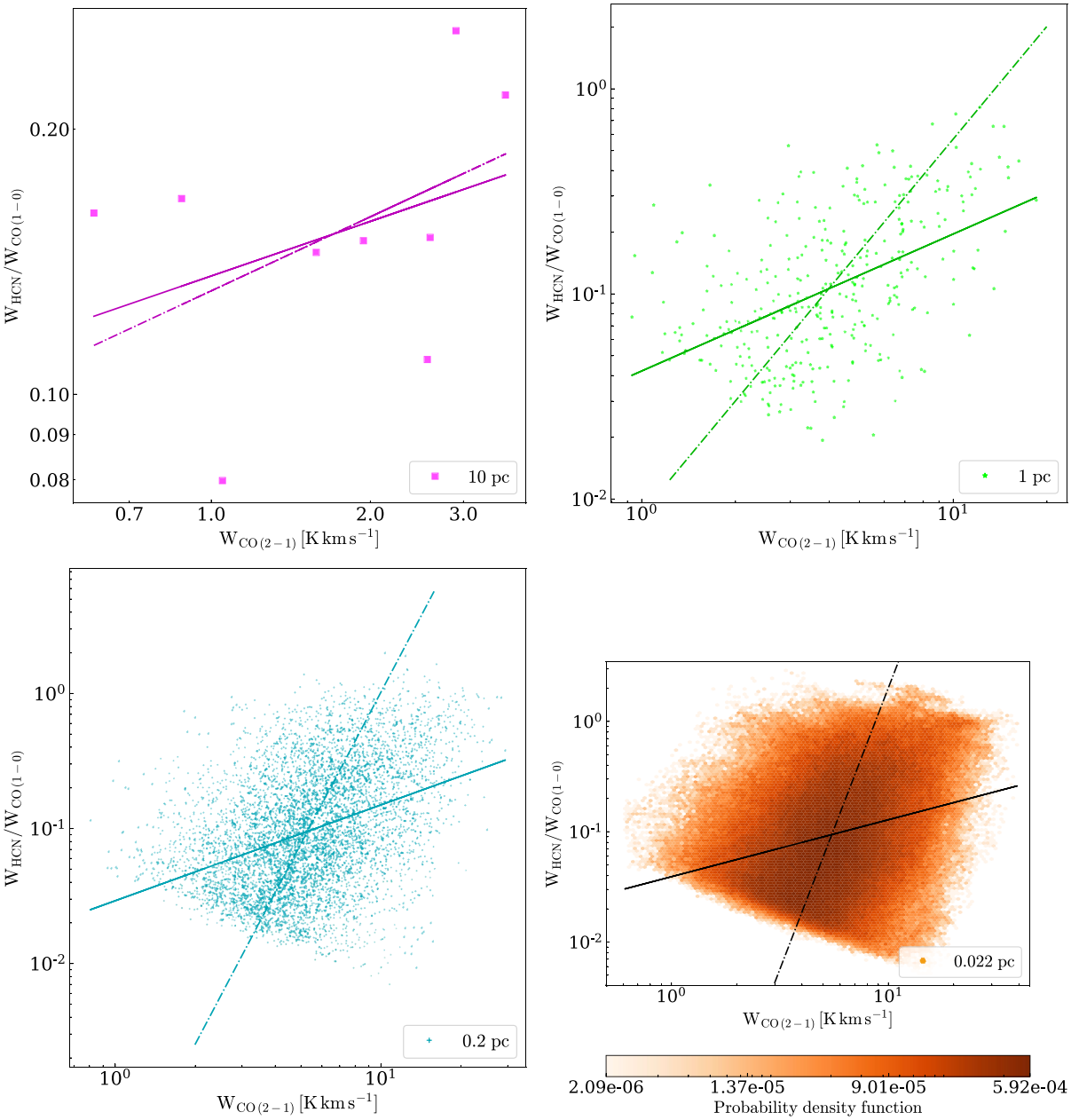

Figure 19. As Fig. 18, but with a higher cut-off of 0.1 K km s^{-1}. The dot–dashed line denotes the gradient obtained through total least squares fitting and the solid line denotes the gradient obtained through ordinary least squares fitting.

the HCN abundance would then be higher than what we currently adopt in these regions (Hacar et al. 2020). This would boost the emission from the lower density gas. The effect on our results would be, if anything, to lower the characteristic density traced by HCN emission, and thus this does not alter our main conclusion. However, whether this combination of effects leads to a linear relation between HCN emission and star formation remains to be tested, and we aim to revisit it in a future study.

Our use of the Fuente et al. (2019) results to derive our HCN to CO abundance ratio also differs slightly from those of Tafalla et al. (2021). Fuente et al. (2019) only observed a particular region of TMC-1 whilst Tafalla et al. (2021) observed the entire cloud. However, using Fuente et al. (2019) gives us a very conservative estimate for the HCN abundance at lower densities (below an A_V of 20 mag) compared to Tafalla et al. (2021). Once again, we can predict that using the Tafalla et al. (2021) abundance ration would almost certainly lower the density threshold (n_{char}) as the higher HCN abundances at lower densities/A_V would provide a greater contribution of HCN emission to our Fig. 9 at lower densities.

The findings in this paper, and those from the observational studies of Pety et al. (2017), Kauffmann et al. (2017), Barnes et al. (2020), and Tafalla et al. (2021) have serious implications for the use of HCN as a tracer of dense gas. This lower density threshold for HCN emission also has implications for the study of the star formation efficiency per free-fall time in GMCs. For example, Krumholz & Tan (2007) argue that star formation in dense gas is 'slow', in the sense that only a small percentage of the gas forms stars every free-fall time. However, they assume that HCN emission traces gas with densities $\sim 6 \times 10^4\,\mathrm{cm^{-3}}$, which therefore has a short free-fall time. If the true value for the density traced by HCN is closer to the value of $\sim 3 \times 10^3\,\mathrm{cm^{-3}}$ that we find; this implies that the actual free-fall time is a factor of 4–5 longer than the value they derive, with a corresponding increase in the inferred star formation efficiency per free-fall time. Further, as we demonstrate at the end of Section 4.2, the commonly-used methods for converting HCN emission into dense gas can overpredict the amount of gas residing at densities of n_{char} and higher orders of magnitude, especially at early times when there is little star formation. This would again artificially lower the apparent star formation rate per free-fall time.

7 CONCLUSIONS

We investigate the relationship between gas density and HCN emission through post-processing of high-resolution magnetohydrodynamical simulations of cloud–cloud collisions using RADMC-3D and AREPO. We carry out four simulations with increasing cloud velocities from 1.875 to 15 $\mathrm{kms^{-1}}$, and study the HCN emission from the clouds at three different times in each simulation, allowing us to explore a wide range of potential molecular cloud environments.

In our study, we find that HCN (1–0) emission traces gas with a characteristic volumetric density of $\sim 3 \times 10^3\,\mathrm{cm^{-3}}$, and a characteristic visual extinction of $\sim$5 mag. Our findings are broadly consistent with those from recent observational studies Pety et al. (2017), Kauffmann et al. (2017), and Barnes et al. (2020), and taken together, implies that HCN emission traces more diffuse gas than previously thought (e.g. Gao & Solomon 2004a).

We also find a luminosity to mass conversion factor of $\alpha_{\mathrm{HCN}}^{A_V} = 6.79\,\mathrm{M_\odot\,(K\,km\,s^{-1}\,pc^2)^{-1}}$ for $A_V > 8$ mag and $\alpha_{\mathrm{HCN}}^{n_{thr}} = 8.62\,\mathrm{M_\odot\,(K\,km\,s^{-1}\,pc^2)^{-1}}$ for $n > 2.85 \times 10^3\,\mathrm{cm^{-3}}$. When we adopt the 'standard' conversion factor with characteristic density $n > 3 \times 10^4\,\mathrm{cm^{-3}}$, we find that the analysis overpredicts the amount of 'dense' gas by at least an order of magnitude. Indeed, in some cases, the conversion factor predicts gas in the the density range $n > 3 \times 10^4\,\mathrm{cm^{-3}}$ when no gas above that density exists in our simulations.

Table 5. Summary of our results of comparison between HCN/CO (1–0) to $W_{CO\,(2-1)}$ for the 0.1 K km s^{-1}. Note that these gradients are obtained through ordinary least squares (OLS) and total least squares (TLS) fitting.

Resolution [pc]	Gradient of fit OLS	TLS
0.022	0.52	5.1
0.2	0.71	3.7
1	0.67	1.83
10	0.21	0.28

ACKNOWLEDGEMENTS

We thank the anonymous reviewer for constructive comments that greatly improved the paper. This research was undertaken using the supercomputing facilities at Cardiff University operated by Advanced Research Computing at Cardiff (ARCCA) on behalf of the Cardiff Supercomputing Facility and the HPC Wales and Supercomputing Wales (SCW) projects. We acknowledge the support of the latter, which is part-funded by the European Regional Development Fund (ERDF) via the Welsh Government'. PCC gratefully acknowledges the support of a STFC Consolidated Grant (ST/K00926/1), and support from the StarFormMapper project, funded by the European Union's Horizon 2020 research and innovation programme under grant agreement No 687528. SCOG acknowledges support from the DFG via SFB 881 'The Milky Way System' (subprojects B1, B2, and B8), from the Heidelberg cluster of excellence EXC 2181-390900948 'STRUCTURES: A unifying approach to emergent phenomena in the physical world, mathematics, and complex data', funded by the German Excellence Strategy, and from the European Research Council via the ERC Synergy Grant 1798 'ECOGAL – Understanding our Galactic ecosystem: From the disc of the Milky Way to the formation sites of stars and planets' (project ID 855130). This project has received funding from the European Research Council (ERC) under the European Union's Horizon 2020 research and innovation programme (Grant agreement Nos. 851435 and 639459).

DATA AVAILABILITY

The data underlying this article will be shared on reasonable request to the corresponding author.

REFERENCES

Barnes A. T. et al., 2020, MNRAS, 497, 1972
Bate M. R., Bonnell I. A., Price N. M., 1995, MNRAS, 277, 362
Bigiel F., Walter F., Blitz L., Brinks E., de Blok W. J. G., Madore B., 2010, ApJ, 140, 1194
Bohlin R. C., Savage B. D., Drake J. F., 1978, ApJ, 224, 132
Clark P. C., Glover S. C. O., Klessen R. S., 2012, MNRAS, 420, 745
Clark P. C., Glover S. C. O., Ragan S. E., Duarte-Cabral A., 2019, MNRAS, 486, 4622
Crutcher R. M., 2012, ARA&A, 50, 29
Crutcher R. M., Wandelt B., Heiles C., Falgarone E., Troland T. H., 2010, ApJ, 725, 466
Dedner A., Kemm F., Kröner D., Munz C. D., Schnitzer T., Wesenberg M., 2002, J. Comput. Phys., 175, 645
Dobbs C. L., 2008, MNRAS, 391, 844

Draine B. T., 1978, ApJS, 36, 595
Draine B. T., 2011, in Draine B. T., ed., Physics of the Interstellar and Intergalactic Medium. Princeton University Press, Princeton
Draine B. T., Bertoldi F., 1996, ApJ, 468, 269
Dullemond C. P., Juhasz A., Pohl A., Sereshti F., Shetty R., Peters T., Commercon B., Flock M., 2012, Astrophysics Source Code Library, record ascl:1202.015
Dumouchel F., Faure A., Lique F., 2010, MNRAS, 406, 2488
Elmegreen B. G., 1994, ApJ, 425, L73
Evans N. J., Kim K.-T., Wu J., Chao Z., Heyer M., Liu T., Nguyen-Lu'o'ng Q., Kauffmann J., 2020, ApJ, 894, 103
Faure A., Varambhia H. N., Stoecklin T., Tennyson J., 2007, MNRAS, 382, 840
Federrath C., 2015, MNRAS, 450, 4035
Federrath C., Banerjee R., Clark P. C., Klessen R. S., 2010, ApJ, 713, 269
Fuente A. et al., 2019, A&A, 624, A105
Gallagher M. J. et al., 2018, ApJ, 868, L38
Gao Y., Solomon P. M., 2004a, ApJS, 152, 63
Gao Y., Solomon P. M., 2004b, ApJ, 606, 271
Gao Y., Carilli C. L., Solomon P. M., Bout P. A. V., 2007, ApJ, 660, L93
García-Burillo S., Usero A., Alonso-Herrero A., Graciá-Carpio J., Pereira-Santaella M., Colina L., Planesas P., Arribas S., 2012, A&A, 539, A8
Glover S. C. O., Clark P. C., 2012, MNRAS, 421, 9
Glover S. C. O., Mac Low M.-M., 2007, ApJ, 659, 1317
Habing H. J., 1968, Bull. Astron. Inst. Neth., 19, 421
Hacar A., Bosman A. D., van Dishoeck E. F., 2020, A&A, 635, A4
Harada N., Nishimura Y., Watanabe Y., Yamamoto S., Aikawa Y., Sakai N., Shimonishi T., 2019, ApJ, 871, 238
Hunter G. H., Clark P. C., Glover S. C. O., Klessen R. S., 2021, MNRAS, 519, 4152
Jankowski P., Szalewicz K., 2005, J. Chem. Phys., 123, 104301
Kainulainen J., Beuther H., Henning T., Plume R., 2009, A&A, 508, L35
Kauffmann J., Goldsmith P. F., Melnick G., Tolls V., Guzman A., Menten K. M., 2017, A&A, 605, L5
Kennicutt R. C., Jr, 1989, ApJ, 344, 685
Kennicutt R. C., Evans N. J., 2012, ARA&A, 50, 531
Kruijssen J. M. D., Longmore S. N., Elmegreen B. G., Murray N., Bally J., Testi L., Kennicutt R. C., Jr, 2014, MNRAS, 440, 3370
Krumholz M. R., Tan J. C., 2007, ApJ, 654, 304
Krumholz M. R., Thompson T. A., 2007, ApJ, 669, 289
Lada C. J., Lombardi M., Alves J. F., 2010, ApJ, 724, 687
Lada C. J., Forbrich J., Lombardi M., Alves J. F., 2012, ApJ, 745, 190
Leroy A. K. et al., 2017, ApJ, 835, 217
Longmore S. N. et al., 2013, MNRAS, 429, 987
Mathis J. S., Mezger P. G., Panagia N., 1983, A&A, 128, 212
Nguyen Q.-R., Jackson J. M., Henkel C., Truong B., Mauersberger R., 1992, ApJ, 399, 521
Onus A., Krumholz M. R., Federrath C., 2018, MNRAS, 479, 1702
Pakmor R., Bauer A., Springel V., 2011, MNRAS, 418, 1392
Pety J. et al., 2017, A&A, 599, A98
Powell K. G., Roe P. L., Linde T. J., Gombosi T. I., De Zeeuw D. L., 1999, J. Comput. Phys., 154, 284
Priestley F. D., Whitworth A. P., 2020, MNRAS, 499, 3728
Priestley F. D., Whitworth A. P., 2021, MNRAS, 506, 775
Querejeta M. et al., 2019, A&A, 625, A19
Riechers D. A., Walter F., Carilli C. L., Weiss A., Bertoldi F., Menten K. M., Knudsen K. K., Cox P., 2006, ApJ, 645, L13
Schmidt M., 1959, ApJ, 129, 243
Schöier F. L., van der Tak F. F. S., van Dishoeck E. F., Black J. H., 2005, A&A, 432, 369
Sembach K. R., Howk J. C., Ryans R. S. I., Keenan F. P., 2000, ApJ, 528, 310
Shetty R., Glover S. C., Dullemond C. P., Klessen R. S., 2011, MNRAS, 412, 1686
Shetty R., Kelly B. C., Rahman N., Bigiel F., Bolatto A. D., Clark P. C., Klessen R. S., Konstandin L. K., 2014, MNRAS, 437, L61
Shirley Y. L., 2015, PASP, 127, 299
Sobolev V. V., 1957, SvA, 1, 678
Springel V., 2010, MNRAS, 401, 791
Tafalla M., Usero A., Hacar A., 2021, A&A, 646, A97
Tress R. G., Smith R. J., Sormani M. C., Glover S. C. O., Klessen R. S., Mac Low M.-M., Clark P. C., 2020, MNRAS, 492, 2973
Weinberger R., Springel V., Pakmor R., 2020, ApJS, 248, 32
Wollenberg K. M. J., Glover S. C. O., Clark P. C., Klessen R. S., 2020, MNRAS, 494, 1871
Wong T., Blitz L., 2002, ApJ, 569, 157
Wu J., Evans II N. J., Gao Y., Solomon P. M., Shirley Y. L., Vanden Bout P. A., 2005, ApJ, 635, L173
Yang B., Stancil P. C., Balakrishnan N., Forrey R. C., 2010, ApJ, 718, 1062

This paper has been typeset from a TEX/LATEX file prepared by the author.